$^3\overrightarrow{\mathrm{He}}(\vec{e}, e')$ quasielastic asymmetry

C. E. Jones,* E. J. Beise, J. E. Belz, R. W. Carr, B. W. Filippone,
W. Lorenzon,† R. D. McKeown, B. A. Mueller, and T. G. O'Neill
W. K. Kellogg Radiation Laboratory, California Institute of Technology, Pasadena, California 91125

G. W. Dodson, K. Dow, M. Farkhondeh, S. Kowalski, K. Lee, N. Makins,
R. Milner, A. Thompson,‡ D. Tieger, J. F. J. van den Brand,§ A. Young,**
X. Yu, and J. D. Zumbro††
Bates Linear Accelerator Center, Laboratory for Nuclear Science and Department of Physics, Massachusetts Institute of Technology, Cambridge, Massachusetts 02139
(Received 11 September 1992)

Measurements of the spin-dependent asymmetry in scattering longitudinally polarized electrons from polarized ^{3}He at quasielastic kinematics are reported. The measurements were made at two kinematics and spin angles, one sensitive to the helicity-dependent transverse-longitudinal interference response function, $R_{TL'}$, and the other to the helicity-dependent transverse response function, $R_{T'}$. For the experiment a metastability exchange optically pumped polarized ^{3}He target was used; a general discussion of the technique used to polarize the ^{3}He, along with the details of the design and operation of the target system, are presented here. A comparison is made of the world's data on the $^3\overrightarrow{\mathrm{He}}(\vec{e}, e')$ quasielastic asymmetry with several theoretical predictions, including calculations that use the plane wave impulse approximation and a fully spin-dependent spectral function. There is good agreement between data and theory at the current level of experimental precision.

PACS number(s): 24.70.+s, 25.10.+s, 25.30.Fj, 29.25.Pj

I. INTRODUCTION

Among the experimental techniques used to probe nuclear structure, electron scattering stands out in terms of the quality of information it provides about the electromagnetic structure of nuclei and nucleons. Until recently, the low luminosity attainable with polarized beams and targets limited electron scattering experiments primarily to unpolarized studies. However, recent advancements in both beam and target technologies make feasible experiments that use polarization degrees of freedom for more complete studies of electromagnetic and electroweak properties. As a result, spin-dependent electron scattering has evolved into a significant part of the physics program at a number of accelerator facilities.

One of the nuclei currently receiving much attention for polarized studies is ^{3}He. The interest arises because of theoretical predictions that in the quasielastic scattering region the spin-dependent properties are dominated by the neutron within the nucleus [1], a phenomenon that occurs because the ^{3}He wave function is predominantly a spatially symmetric S state in which the protons occupy a spin-singlet state. Therefore, experimental studies of polarized ^{3}He can provide information about the electromagnetic properties of the neutron. Although detailed studies of the proton have been pursued for several decades, much less is known of the neutron electromagnetic properties because free neutrons beta decay with such a short half-life that they cannot be made into a dense target. Our current knowledge of the neutron electric form factor is rather limited: Only the slope of G_E^n at zero four-momentum transfer squared ($Q^2 = 0$) is well determined [2]. The bulk of our knowledge about the Q^2 dependence of G_E^n comes from unpolarized scattering experiments using deuterium targets, which are subject to uncertainties because of the sensitivity to the deuteron wave function and the large corrections for the proton contribution to the cross section.

New techniques to measure G_E^n are needed, and measurements that use polarization observables to enhance the sensitivity to the neutron properties are an attractive alternative. One such technique is the use of longitudinally polarized electrons and polarized ^{3}He mentioned above. For inclusive quasielastic scattering with both beam and target polarized, the cross section contains a term dependent upon the interference between the charge and magnetic matrix elements that enhances the contribution from the neutron electric form factor. If the ^{3}He ground state were entirely a symmetric S state, then the spin of the nucleus would be carried solely by the neutron.

*Current address: Physics Division, Argonne National Lab, Argonne, IL 60439.
†Current address: TRIUMF, Vancouver, BC V6T 2A3, Canada.
‡Current address: Physics Department, Harvard University, Cambridge, MA 02138.
§Current address: Physics Department, University of Wisconsin, Madison, WI 53706.
**Current address: Physics Department, Arizona State University, Tempe, AZ 85287.
††Current address: Los Alamos Meson Physics Facility, Los Alamos, NM 87545.

In this case, measurements of spin-dependent quantities in quasielastic scattering would be sensitive to neutron electromagnetic form factors without background from the protons, which would contribute only to the unpolarized cross section. In reality, because of the small admixture of other states in the ^{3}He wave function, the protons also contribute to the spin-dependent cross section and should be taken into account when extracting information about the electromagnetic properties of the neutron.

The experiment described here, the first to use a polarized ^{3}He target and a polarized electron beam, is a measurement of the spin-dependent asymmetry in inclusive quasielastic scattering. The experiment was performed at the MIT-Bates Linear Accelerator Center using 574 MeV longitudinally polarized electrons and a polarized ^{3}He target designed and built at Caltech. Data were collected in two spectrometers to obtain asymmetry measurements that contain complementary information about the neutron form factors, with one asymmetry sensitive to G_E^n and the other sensitive to G_M^n. The results have been published previously [3]; this paper provides more complete information about the data analysis and the final results, along with a detailed description of the polarized ^{3}He target, which uses metastability exchange optical pumping to orient the nuclei in a small holding field.

II. THEORETICAL OVERVIEW

The detailed formalism for inclusive electron scattering including polarization degrees of freedom is given by Donnelly and Raskin [4]. Although they treat the general case where the electron is polarized in an arbitrary direction, we restrict ourselves to the experimentally interesting case where the electrons are longitudinally polarized, with helicity h. We also consider only a spin-$\frac{1}{2}$ target, for which the formalism simplifies even further.

In general, the target spin can be oriented in any direction; the spin direction $\mathbf{S}$ is specified relative to the direction of the three-momentum transfer $\mathbf{q}$ by the two Euler angles θ^* and ϕ^*, where $\cos\theta^* = \mathbf{S}\cdot\mathbf{q}/|\mathbf{q}|$ and ϕ^* is the angle between the electron scattering plane and the plane containing $\mathbf{S}$ and $\mathbf{q}$. The expressions for the cross section are derived assuming the Born approximation, a single-photon-exchange interaction, and the extreme relativistic limit for the electrons. The kinematic dependence is expressed in terms of the electron scattering angle θ, the energy transfer ω, the three-momentum transfer $\mathbf{q}$, and $Q^2 \equiv |\mathbf{q}|^2 - \omega^2$. For quasielastic scattering from a spin-$\frac{1}{2}$ particle, the differential cross section separates into two terms, one that is independent of the polarizations of the beam and target and one that contributes only if both beam and target are polarized. Typically, the cross section is written in terms of quasielastic response functions, which depend upon Q^2 and ω and contain the information about the electromagnetic structure of the target:

$$\frac{d^2\sigma}{d\Omega dE} = \Sigma + h\Delta, \tag{1}$$

where

$$\Sigma = \sigma_{\text{Mott}}\left[v_L R_L(Q^2,\omega) + v_T R_T(Q^2,\omega)\right] \tag{2}$$

and

$$\Delta = -\sigma_{\text{Mott}}[\cos\theta^* v_{T'} R_{T'}(Q^2,\omega) + 2\sin\theta^*\cos\phi^* v_{TL'} R_{TL'}(Q^2,\omega)]. \tag{3}$$

σ_{Mott} is the Mott cross section and the v_K are kinematic factors defined as

$$v_L = \left(\frac{Q^2}{|\mathbf{q}|^2}\right)^2, \tag{4}$$

$$v_T = \frac{1}{2}\left(\frac{Q^2}{|\mathbf{q}|^2}\right) + \tan^2\frac{\theta}{2}, \tag{5}$$

$$v_{T'} = \tan\frac{\theta}{2}\sqrt{\left(\frac{Q^2}{|\mathbf{q}|^2}\right) + \tan^2\frac{\theta}{2}}, \tag{6}$$

$$v_{TL'} = -\frac{1}{\sqrt{2}}\left(\frac{Q^2}{|\mathbf{q}|^2}\right)\tan\frac{\theta}{2}. \tag{7}$$

The R_L response function contains Coulomb matrix elements only, and R_T and $R_{T'}$ depend only upon products of transverse electromagnetic matrix elements, while $R_{TL'}$ results from the interference of Coulomb and transverse matrix elements.

The spin-dependent asymmetry is the ratio of the helicity-dependent term in the cross section to the helicity-independent term,

$$A = \frac{\left(\frac{d^2\sigma}{d\Omega dE}\right)_+ - \left(\frac{d^2\sigma}{d\Omega dE}\right)_-}{\left(\frac{d^2\sigma}{d\Omega dE}\right)_+ + \left(\frac{d^2\sigma}{d\Omega dE}\right)_-} = \frac{\Delta(\theta^*,\phi^*)}{\Sigma}, \tag{8}$$

where $+(-)$ denotes the helicity of the incident electron. Expressed in terms of the quasielastic response functions, the asymmetry is

$$A = -\frac{\cos\theta^* v_{T'} R_{T'}(Q^2,\omega) + 2\sin\theta^*\cos\phi^* v_{TL'} R_{TL'}(Q^2,\omega)}{v_L R_L(Q^2,\omega) + v_T R_T(Q^2,\omega)}. \tag{9}$$

In practice, the asymmetry that one measures experimentally is reduced from the value given above by the degree of polarization of the target and beam,

$$A_{\text{expt}} = P_t P_e A. \tag{10}$$

The sensitivity of A_{expt} to each spin-dependent response function can be optimized by varying θ^*, the angle between the nuclear spin and $\mathbf{q}$. For the case where the target polarization axis is in the scattering plane, if $\theta^* = 0°$, then the asymmetry is maximally sensitive to $R_{T'}$, and if

$\theta^* = 90°$, the asymmetry is maximally sensitive to $R_{TL'}$. The spin-dependent quasielastic response functions of ^{3}He are predicted to be quite sensitive to the electromagnetic form factors of the neutron [1]. In particular, $R_{T'}$ depends primarily upon $(G_M^n)^2$ and $R_{TL'}$ depends upon $(G_E^n G_M^n)$.

The ^{3}He ground state wave function is predominantly S state, with small admixtures of approximately 8% D state and 2% S' state. The S state is a spatially symmetric, spin-isospin antisymmetric state in which the protons' spins are coupled to spin 0 and the neutron carries the ^{3}He nuclear spin. The S' state is an $L = 0$ mixed symmetry state that arises because of the spin dependence of the nucleon-nucleon interaction. The D state is an $L = 2$ state in which the nucleon spins are oriented predominantly opposite the orbital angular momentum. Both the S'- and D-state components dilute the fraction of the nuclear spin carried by the neutron.

A simple model of the contribution of the neutron within ^{3}He to the spin-dependent asymmetry has been suggested by Friar *et al.* [5]. They estimate the fraction of the polarization carried by the neutrons in a sample of 100% polarized ^{3}He, using ground state wave functions obtained from a number of different nuclear potential models and constraining the results with the experimental binding energy of ^{3}He. They suggest that the ^{3}He quasielastic asymmetry can be approximated by

$$A = (1 - 2\delta)\left(\frac{\sigma_n}{\sigma_n + 2\sigma_p}\right) A_{en} - 2\delta'\left(\frac{2\sigma_p}{\sigma_n + 2\sigma_p}\right) A_{ep}, \tag{11}$$

In this model, the ^{3}He asymmetry is decomposed into the contributions from the free nucleon asymmetries for the proton and the neutron, diluted by the relative cross sections and the fraction of the nuclear spin carried by each. δ and δ' depend upon the state probabilities of the ^{3}He ground state wave function, $\delta = [2\mathcal{P}(D) + \mathcal{P}(S')]/3$ and $\delta' = [\mathcal{P}(D) - \mathcal{P}(S')]/6$. They estimate $\delta = 0.07 \pm 0.01$ and $\delta' = 0.014 \pm 0.002$, where the error bar reflects the uncertainty due to nuclear structure effects. A_{en} and A_{ep} depend only upon the free nucleon form factors and kinematic factors, and can be written in terms of the Sachs form factors as

$$A_{eN} = -\frac{2\tau v_{T'} \cos\theta^* (G_M^N)^2 - 2\sqrt{2\tau(1+\tau)} v_{TL'} \sin\theta^* \cos\phi^* (G_M^N)(G_E^N)}{(1+\tau) v_L (G_E^N)^2 + 2\tau v_T (G_M^N)^2}, \tag{12}$$

where $\tau \equiv Q^2/4m_N^2$. This model does not predict the ω dependence of the asymmetry; the S, S', and D states are assumed to be equally sampled by all quasielastic scattering events. Despite this limitation, the model gives a physically intuitive description of ^{3}He. Perhaps the most important feature of the model of Friar *et al.*, though, is that it provides an estimate of the magnitude of the uncertainty from nuclear structure effects in theoretical calculations of the ^{3}He asymmetry by using different potentials in the calculation.

More realistic calculations of the ^{3}He quasielastic asymmetry are available. In Ref. [1], Blankleider and Woloshyn estimate the effect of the protons on the quasielastic asymmetry using the ^{3}He ground state wave function of Afnan and Birrell [6], obtained by solving Faddeev equations with the Reid soft-core potential. For the calculations they model quasielastic electron scattering in the plane wave impulse approximation. Rather than using a spectral function for ^{3}He, which would include both Fermi momentum and binding energy effects, they make a closure approximation to sum over final states so that they use a spin-dependent momentum distribution to calculate the nuclear effects. Figure 1 shows the ^{3}He quasielastic asymmetry as a function of ω for $E = 574$ MeV, $\theta = 44°$, and $Q^2 = 0.158$ (GeV/c)^2, calculated following Blankleider and Woloshyn. The asymmetries for $\theta^* = 0°$ ($A \propto R_{T'}$)and $\theta^* = 90°$ and $\phi^* = 0°$ ($A \propto R_{TL'}$) are shown separated into contributions from the protons and the neutron. The relative contribution from the protons is smaller for $\theta^* = 0°$ where, within the model of polarized ^{3}He primarily as a polarized neutron, the asymmetry is dominated by the magnetic form factor

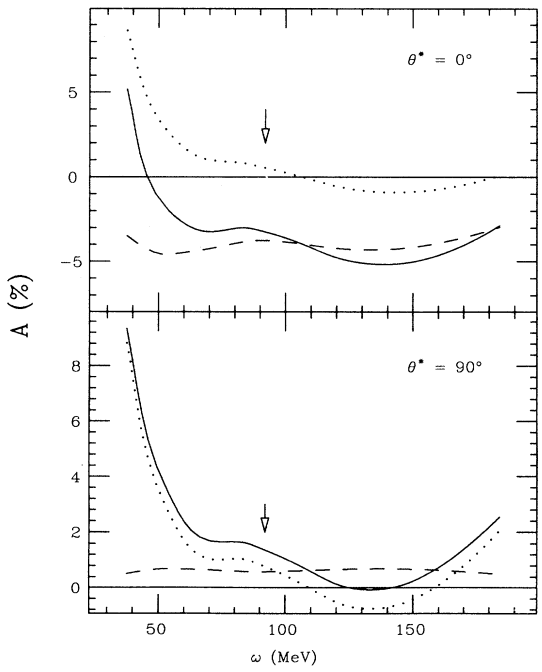

FIG. 1. Calculated ^{3}He quasielastic asymmetry (solid line) as a function of energy transfer for $E = 574$ MeV and $\theta = 44°$, using the formalism of Blankleider and Woloshyn. The upper graph is the asymmetry for $\theta^* = 0°$, and the lower is for $\theta^* = 90°$. The contributions from the protons (dots) and neutrons (dashes) are shown. The top of the quasielastic peak is indicated by the arrow.

of the neutron. At the top of the quasielastic peak, the proton contribution is relatively small. For $\theta^* = 90°$, the calculation indicates that the proton contribution is comparable to that of the neutron over much of the quasielastic peak, and that it dominates in the tails of the peak.

Recently, calculations of the asymmetry in the $^3\vec{\text{He}}(\vec{e},e')$ reaction were made using a fully spin-dependent spectral function calculated with the Reid soft-core interaction [7]. Ciofi degli Atti, Pace, and Salmè studied the validity of the closure approximation made by Blankleider and Woloshyn, the size of the proton contribution to the asymmetry as a function of energy and momentum transfer, and the dependence of the asymmetry on the nucleon form factors. They find that the closure approximation gives results that differ by as much as 100% from the full calculation in the tails of the quasielastic peak where the S' and D states dominate the asymmetry. They also find smaller differences between the asymmetries at the top of the quasielastic peak calculated with the two methods. The differences tend to become less significant at higher Q^2.

Theoretical calculations of the ^{3}He quasielastic asymmetry so far have been done only within the plane wave impulse approximation, although calculations including final state interactions are planned [8]. Experimental data exist for the unpolarized inclusive quasielastic scattering cross section [9], and calculations including final state interactions have been done and compared to these results [10]. The comparison indicates that the spin-independent longitudinal response function R_L is well described when final state interaction effects are included. The experimental data for the transverse response function R_T are adequately described by the plane wave impulse approximation. The calculation including final state interactions underestimates R_T, suggesting that meson exchange currents may be needed to explain the data. Experimental data from polarized quasielastic electron scattering, combined with asymmetry calculations that include final state interactions and meson exchange currents, could give information needed to clarify the reaction process.

III. EXPERIMENTAL OVERVIEW

Quasielastically scattered electrons were detected in two magnetic spectrometers, OHIPS and BIGBITE, located in the South Experimental Hall of the MIT-Bates Linear Accelerator Center. The target contained 2.1 torr polarized ^{3}He gas, cooled to 16.7 K, with the nuclei polarized through metastability exchange between the ground state ^{3}He atoms and optically pumped 2^3S_1 metastable atoms. The target cell had an effective target length seen by the spectrometers of 10 cm, corresponding to a target thickness of $1.2 \times 10^{19}/\text{cm}^2$. Because the polarized ^{3}He target design is new, it is described in detail in Sec. IV while the other aspects of the experiment are discussed here.

A beam of longitudinally polarized electrons at 574 MeV incident energy, obtained from a conventional GaAs source [11], was used for the experiment. The typical peak current at the target was 1 mA, with a pulse rate of 600 Hz and pulse length of 15 μsec. The beam energy was known to a precision of 1% and was chosen to provide longitudinally polarized electrons at the target chamber after spin precession through the bending magnets in the beam transport system. The electron helicity was varied randomly on a pulse-by-pulse basis. The beam polarization, measured with a Møller polarimeter upstream of the target chamber [12], was $P_e = 40.5 \pm 4.2\,\%$.

The layout of the experimental apparatus is shown in Fig. 2. Inclusive measurements of the scattered electrons were made independently in the two detector arms. Table I contains a summary of the kinematics for the measurements. OHIPS was placed at an angle of 51.1°, with the central momentum of the spectrometer set to correspond to the center of the quasielastic peak (462 MeV). The solid angle of OHIPS for the extended target was 12.2 msr and the momentum acceptance was ±5%, measured with elastic scattering from a ^{12}C target. The BIGBITE spectrometer, located at an angle of 44.0°, had a sufficiently large momentum acceptance (±25%) to detect both elastic events and a large part of the quasielastic spectrum. The central momentum of the spectrometer was 517 MeV, which corresponds to placing the center of the quasielastic peak at $\delta p/p_0 \sim -5\%$. Because the momentum analysis of the BIGBITE spectrometer is done by bending the particles in the scattering plane, the momentum resolution is poor for an extended target. For a 10-cm-long target viewed at 44°, the momentum resolution is ±3.5% full width at half maximum (FWHM). The solid angle of BIGBITE is calculated to be 7.1 msr using the Monte Carlo program TURTLE [13]. In general, knowledge of the spectrometer acceptance is not critical for an asymmetry measurement because to first order spectrometer properties cancel in the ratio of the cross sections.

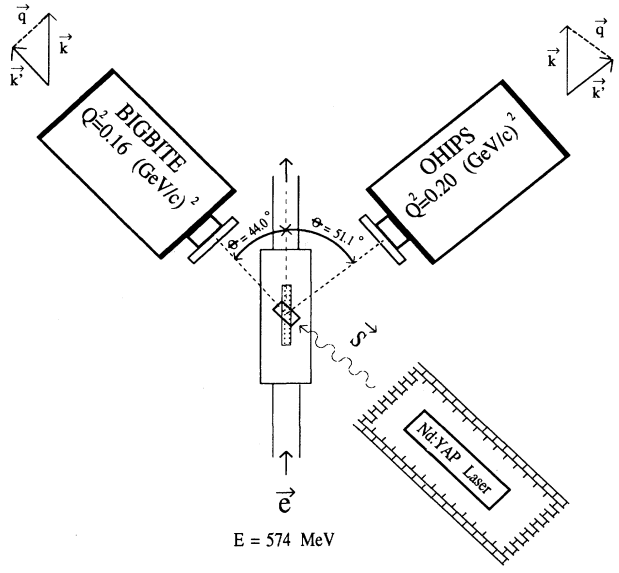

FIG. 2. Layout of the spectrometers and the laser used for optical pumping. The kinematics of the quasielastic events detected by each spectrometer are indicated on the drawing.

TABLE I. Kinematics of the OHIPS and BIGBITE measurements at the top of the quasielastic peak.

Spectrometer	θ (deg)	Q^2 (GeV/c)^2	$\|\mathbf{q}\|$ (MeV/c)	$\theta_\mathbf{q}$ (deg)
OHIPS	51.1	0.20	460	−52.4
BIGBITE	−44.0	0.16	406	56.9

The unpolarized cross section was calculated from the experimental data and compared with previous measurements in the same kinematic region as a check on our determination of the target thickness. The experimental cross sections agree with previous ^{3}He quasielastic measurements [9] that are scaled to the appropriate kinematics using y scaling [14] within the systematic uncertainty of ±10% (primarily due to spectrometer acceptance) in the extracted cross sections.

The target spin was oriented in three different directions over the course of the experiment. In all cases the spin axis lay in the scattering plane. The directions, specified in terms of β, where $\cos\beta = \mathbf{S}\cdot\mathbf{k}_i/|\mathbf{k}_i|$, where $\mathbf{k}_i$ is the incident electron momentum, were $\beta = -51.5°$, $-44.5°$, and $+135.5°$. In this notation, the plus sign indicates angles to beam right. The first orientation corresponds to $\theta^* = 0.9°$ for the OHIPS quasielastic kinematics and $\theta^* = 108.4°$ for BIGBITE kinematics. The second orientation was chosen to make the BIGBITE measurement more sensitive to G_E^n and yet has little effect on the sensitivity of the OHIPS measurement to G_M^n. Finally, the spin direction was reversed to check for systematic errors.

IV. POLARIZED ^{3}He TARGET

The polarized ^{3}He target makes use of a technique developed in the early 1960s by Colegrove, Schearer, and Walters [15], whereby ground state ^{3}He nuclei are polarized through metastability exchange collisions with optically pumped ^{3}He metastable atoms. Recently intense laser sources of optical pumping light at the wavelength of the $2^3S \rightarrow 2^3P$ transition in ^{3}He ($\lambda = 1.0834$ μm) [16] became commercially available, making feasible polarized ^{3}He targets of sufficiently high polarization and density for electron scattering experiments. The target described here is a two-cell closed system for use as an external target. The target density is increased by optically pumping the ^{3}He in a cell at room temperature and using another cell, cooled to cryogenic temperature and connected by diffusive transfer to the pumping cell, as the target cell.

In this target, the ^{3}He atoms are present as an isotopically and chemically pure polarized species. This is especially important for quasielastic scattering experiments where the total number of nucleons is relevant and other nuclear species present in the target contribute to the background under the ^{3}He quasielastic peak. The purity of the gas eliminates the need for kinematic unfolding of the dilution of the asymmetry due to the presence of other polarized or unpolarized nuclear species; such dilution is a significant source of systematic error.

The ^{3}He target can be rapidly polarized, on the time scale of several minutes, using metastability exchange optical pumping. The ability to rapidly polarize a sample of pure ^{3}He makes this technique ideal for internal targets where the polarized gas flows through a windowless target cell [17]. The optical pumping procedure works as follows: The metastable 2^3S_1 population is produced using a weak rf discharge ($f \approx 200$ kHz) in a cell of ^{3}He gas at a pressure of order 1 torr. The ratio of ground state atoms to 2^3S_1 atoms is approximately 10^6:1; the exact value depends upon the discharge level. The cell is placed in a homogeneous magnetic field with the **B** field direction defining the spin quantization axis. For the target, Helmholtz coils were used for the **B** field so that the spin orientation was easily changed by rotating the coils. Circularly polarized light at the wavelength of the $2^3S_1 \rightarrow 2^3P_0$ atomic transition, incident upon the ^{3}He atoms, induces $\Delta m = +(-)1$ transitions for right-handed (left-handed) circularly polarized light, where m is the magnetic quantum number. The electronic polarization is transferred to the nucleus through the hyperfine interaction. The 2^3P_0 state decays through photon emission with equal probability to any accessible state, and repeated absorption and emission polarize the 2^3S_1 metastable atoms. The polarization is transferred to the ground state nuclei through metastability exchange collisions, which exchange the excitation of the atomic electrons without altering the nuclear spins of the atoms involved. The collision process can be written schematically as

$$^3\overrightarrow{\mathrm{He}}(2^3S_1) + {}^3\mathrm{He}(1^1S_0) \longrightarrow {}^3\overrightarrow{\mathrm{He}}(1^1S_0) + {}^3\mathrm{He}(2^3S_1).$$

The ^{3}He atomic energy levels relevant to the optical pumping process are shown in Fig. 3. The nine lines of the $2^3S \rightarrow 2^3P$ transition are designated by the notation C1–C9. At a pressure of 2 torr, where the target used for this experiment was operated, collisional depolarization in the 2^3P state is important and higher polarizations are attained by optical pumping on the C8 and C9 lines [18]. The optical pumping technique is limited to relatively low pressures, $\sim 0.1 - 10$ torr. At the lower end of this pressure range, the attainable polarization is limited by collisions with the walls of the container, which cause spin relaxation, and at the higher pressures the lifetime of the metastable atoms limits the efficiency. The metastability

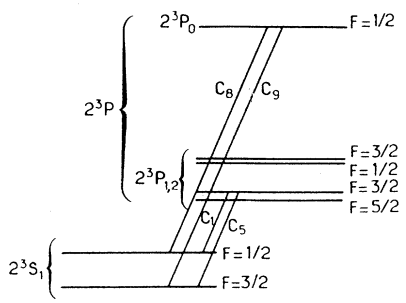

FIG. 3. Level diagram for the 2^3S and 2^3P states of ^{3}He.

exchange cross section is a strong function of the temperature, with the exchange rate decreasing approximately two orders of magnitude between room temperature and liquid helium temperature [19]. For this reason, although the target cell can be cooled to cryogenic temperatures, the pumping cell is operated at room temperature for better ground state polarization efficiency. The density of the target can be increased by either cooling the target cell, as is done with the system described here, or compressing the gas after optical pumping [20].

The polarized ^{3}He target is shown schematically in Fig. 4. It is a double-cell system with a Pyrex pumping cell at room temperature connected via a Pyrex transfer tube to a cooled copper target cell through which the beam passes. Since the target cell is constructed of metal, it is mechanically, thermally, and electromagnetically robust in the presence of a high-intensity electron beam. The pumping cell, a Pyrex cylinder 5 cm in diameter by 10 cm long, is located outside the scattering chamber and is connected by a Teflon-glass valve to the gas inlet system. Four discharge loops encircling the pumping cell produce the weak discharge that creates the metastable atoms. The transfer tube has an inner diameter of 0.93 mm and is epoxied (Stycast 2850GT with catalyst LV24) to the target cell. The target cell is made of a 16-cm-long OFHC copper cylinder of inner diameter 2.54 cm and thickness 0.25 mm, with 4.6 μm copper foil windows epoxied at both ends. The target cell is attached to a Cryomech GB04 closed-cycle helium refrigerator by copper braids, which provide mechanical flexibility during cooling. Carbon-glass temperature sensors, used to monitor the target temperature, are mounted at the middle and end of the cell. The scattering chamber is made of 6061 Al and has 0.25-mm-thick Al exit windows along the sides. To ensure that electrons scattered from the entrance and exit windows were not detected by the spectrometers, 2.54-cm-thick tungsten collimators were placed outside the exit windows to restrict the effective target length seen by the spectrometers to 10 cm. Encircling the scattering chamber were coils in a near Helmholtz configuration that generated a magnetic holding field of 18 G at the center of the coils. The magnetic field direction, which serves as the spin quantization axis, was determined to a precision of $\pm 0.5°$. The target was operated at a gas pressure in the range from 1.95 to 2.15 torr; the temperature monitor provided information about the target pressure variations. The temperature without beam on target was $\sim$ 16 K and rose about 1 K with 15 μA of beam current. The change in temperature from beam heating of the target caused less than 1% change in the fraction of atoms in the target cell.

The laser and polarizing optics are shown in Fig. 5. The laser that provided the optical pumping light contains a YAP crystal in an elliptical cavity with the crystal at one focus and a krypton arc lamp at the other focus. The laser operates in cw mode. The YAP crystal, doped with 0.7% neodymium, is 4 mm diameter by 79 mm long, with the a crystalline axis along the rod axis. A birefringent filter and a 0.25-mm-thick uncoated glass étalon are used to tune from the primary frequency of the Nd:YAP crystal, which corresponds to 1.0795 μm light, to 1.0834 μm, the wavelength of the metastable transition. The coarse frequency tune is monitored with a monochrometer, and the fine tuning is done by maximizing the fluorescence of ^{3}He in a sealed cell (0.8 torr) placed outside the laser cavity. The optical pumping light is extracted from the cavity as the loss off the two faces of the birefringent filter. The relative orientation of the birefringent filter and the YAP crystal is chosen so that the light from the laser is linearly polarized along the c crystalline axis. To be circularly polarized, the light passes through a linear polarizer, oriented for maximum transmission, and a quarter-wave plate, oriented at 45° to the linear polarization axis, placed outside the laser cavity. The sense of circular polarization of the pumping light is changed using left and right circular polarizers

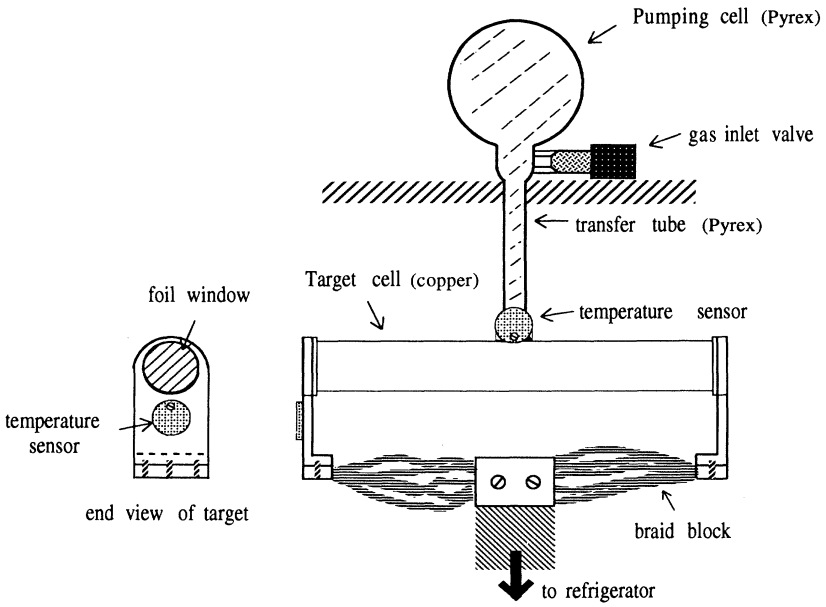

FIG. 4. Schematic of the polarized ^{3}He target double-cell system. The relative positions of the pumping cell, transfer tube, and target cell are shown, in addition to the temperature sensors, gas inlet valve, and the braid block connecting the target cell to a cryogenic refrigerator.

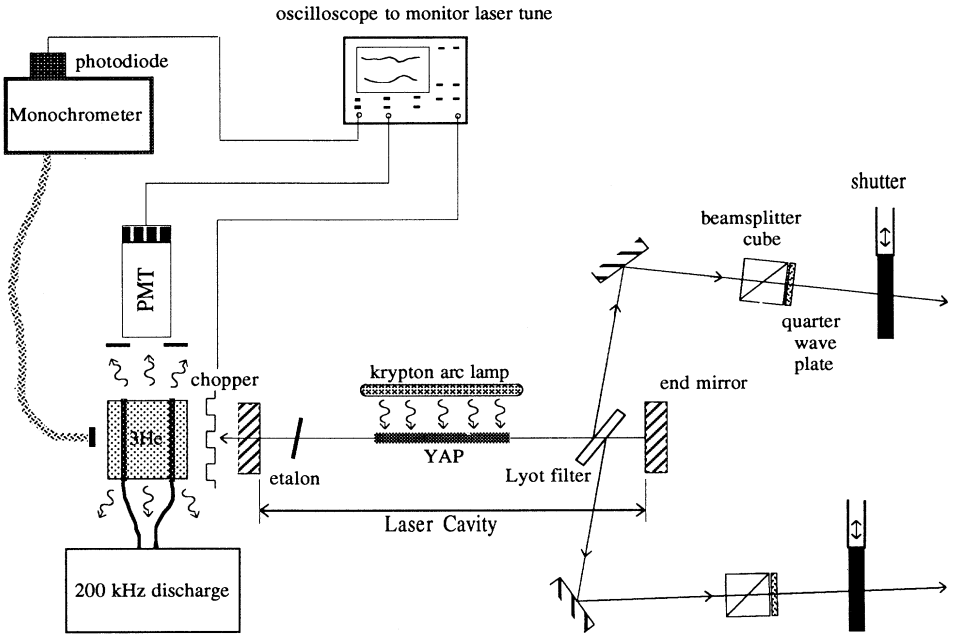

FIG. 5. Schematic of the Nd:YAP laser system, polarizing optics, and laser tuning apparatus.

that are moved mechanically. The laser system used for this experiment provided $\sim$ 300 mW power at the optical pumping frequency. However, currently, systems for ^{3}He metastability exchange optical pumping more commonly use Nd:LMA laser crystals, which to date have provided up to 6 W of optical pumping light [21].

In a double-cell system with the cells in diffusive contact so that the atoms pass back and forth between the two volumes, the target polarization can be determined indirectly from the polarization of the atoms in the pumping cell, which is monitored continuously using an optical technique described below. The polarization of the ^{3}He in the target cell is inferred from the measured polarization of the atoms in the pumping cell using knowledge of the relative volumes of the two cells, the exchange time between the two volumes, and the relaxation time of the coupled system. A discussion of the coupled spin relaxation rate equations for a double-cell system is included in the Appendix. The polarization of the atoms in the pumping cell is measured using a technique that relates the nuclear polarization to the optical polarization of light emitted by excited atomic states. Since the excited state atoms are polarized through the hyperfine interaction between the nucleus and the atomic electrons, the circular polarization of the emitted light is related to the nuclear polarization. The emission from the $3^1D_2 \rightarrow 2^1P_1$ transition, at $\lambda = 668$ nm, is used to determine the nuclear polarization. A detailed discussion of the technique is found in Ref. [22]. The light is detected and analyzed by an optical polarimeter, consisting of a rotating quarter-wave plate followed by a linear polarizer, which views the pumping cell from outside the Helmholtz coils (see Fig. 6). The optical polarization measurement has been calibrated against a direct measurement of the nuclear polarization using NMR at Caltech [23].

A major concern about any polarized target is the depolarizing influences acting upon the nuclei. Because ^{3}He is inert and therefore is not easily incorporated into molecules, the spin relaxation due to collisions is much smaller than that experienced by other polarized atoms under similar experimental conditions. Therefore, the spin relaxation time constants can be very long under suitable conditions. The major sources of spin relaxation are magnetic field gradients and collisions that tend to disorient the atoms. The depolarizing collisions involve interactions with electrons, ions, excited states, and impurities in the gas, and interactions with atoms at the surface of the container. In general, depolarization from field gradients becomes less important at lower temperatures because the atoms diffuse more slowly throughout the volume, and the surface effects become more important at lower temperatures because the residence time on the wall is longer.

In the pumping cell, the primary source of depolarization is interactions with ions and excited states created by the discharge. Since the discharge is the source of the metastable atoms, which are continuously optically pumped, this mechanism cannot be eliminated. However, the discharge level can be adjusted to optimize the polarization in the target cell; the achievable polarization depends upon both the metastable population density and the spin relaxation rate. Because the pumping cell is at room temperature, depolarization from magnetic field gradients is also important. The two-cell system is placed with the pumping cell closer to the center of the Helmholtz coils to lessen the depolarizing effects of magnetic field gradients.

In the target cell, which is operated at temperatures near 15 K, surface depolarization effects dominate in the absence of beam. ^{3}He depolarization on various surfaces at room temperature has been studied previously [24]. During the design of the target, the temperature dependence of the relaxation rate in the copper target cell was studied at Caltech, both with and without wall coatings

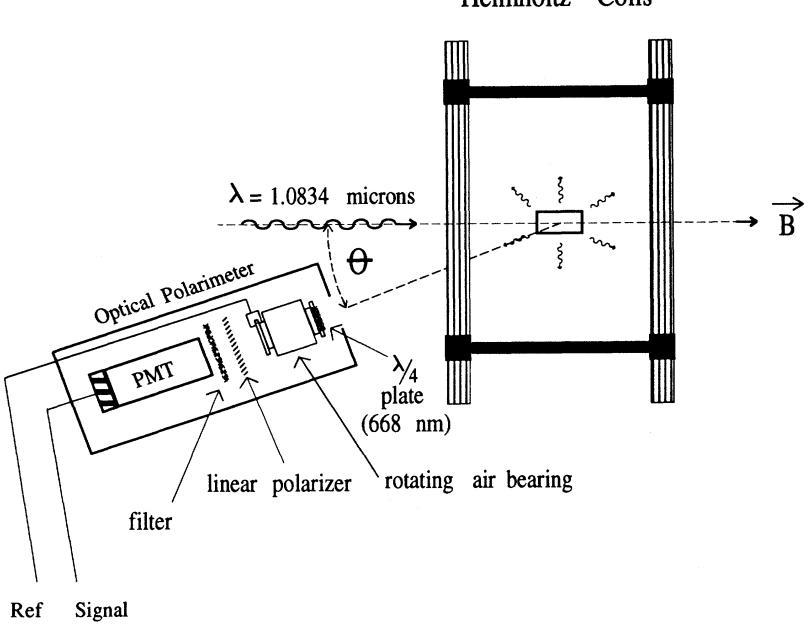

FIG. 6. Optical polarimeter consisting of a rotating quarter-wave plate, linear polarizer, filter, and photomultiplier tube sensitive to 668 nm light from the $3^1D_2 \rightarrow 2^1P_1$ transition. The phototube signal is processed by a lock-in amplifier to extract the circularly polarized component of the light.

of frozen Ar or N_2. The results, shown in Fig. 7, indicate that the surface coating increases the spin relaxation half-life significantly at temperatures below 25 K. No significant difference was noted between Ar and N_2 surface coatings. To alleviate surface depolarization, the target walls were coated with frozen N_2 ($\sim 2 \times 10^{18}/\text{cm}^2$) during operation. Since the target was operated well below the freezing point of the gas, no background from N_2 in the target was seen.

Depolarization effects in the presence of the beam arise from several sources. Here we consider two basic mechanisms that contribute to the spin relaxation. One arises because a charged particle beam generates a magnetic field to which the nuclear spins can couple. The magnitude of this depolarizing effect depends upon the current and pulse structure of the beam, and was negligible for this experiment. The second beam-induced spin relaxation mechanism to be discussed involves the creation of ions by the beam. This is the dominant beam depolarization mechanism for the ^{3}He target at the beam currents used in this experiment. References [25] and [26] present models of spin relaxation from the creation of atomic and molecular ions by an ionizing beam. The nuclei can be depolarized by either ionic species, but for the pressures used for this target the formation of the molecular ions $^3He_2{}^+$ in three-body collisions becomes significant, and effects from molecular ions dominate. The depolarization occurs because the nuclear spins of ^{3}He incorporated into molecular ions couple to the rotational degrees of freedom. At high pressures, recombination with electrons in the gas tends to destroy the molecular ions. At low pressures, the molecular ions are destroyed by collisions with the wall. The energy needed to create an atomic ion is approximately 50 eV/ion. An ionizing beam of particles will create $^3He^+$ ions per unit volume at a rate, in $\text{cm}^{-3}\,\text{sec}^{-1}$, of

$$S_1 \approx 6 \times 10^{12} \left(\frac{Ipl}{VT}\right) \left(\frac{dE}{dx}\right), \tag{13}$$

where I is the beam current (μA), p is the pressure (torr), l the target length (cm), V the target volume (cm^3), T the target temperature (K), and $\frac{dE}{dx}$ the stopping power [MeV/(g/cm^2)]. For minimum ionizing particles incident on ^{3}He, the stopping power is 2.6 MeV/(g/cm^2). From this equation, it is estimated that $\sim 6 \times 10^{14}$ $^3He^+$ ions

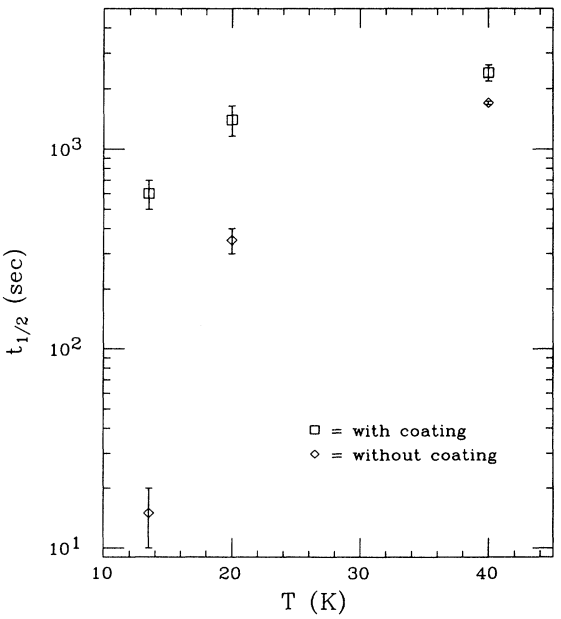

FIG. 7. Target cell relaxation half-life as a function of target temperature, with and without a surface coating of frozen argon in the target cell.

are formed per second for 20 μA of beam current. For this target, the $^3He^+$ atomic ions are converted into $^3He_2{}^+$ molecular ions very rapidly, within approximately 8 μsec. The conversion rate, in $cm^{-3}\,sec^{-1}$, for the atomic ions to become incorporated into molecular ions, written in terms of the atomic ion concentration C, is [26]

$$S_2 = 8.8 \times 10^6 \left(\frac{p}{T}\right)^2 C. \tag{14}$$

For the density used for the target, recombination with electrons is more significant than wall collisions in destroying the molecular ions, and the molecular ions are concentrated near the beam path. In this case, there may be a polarization gradient in the target cell, where the polarization of the ^{3}He in the beam path is different from the average polarization in the cell. One estimates the size of the effect from information about the diffusion time of the ^{3}He atoms in the target cell and the measured values of the contribution to the relaxation rate from the beam. The beam relaxation time for 20 μA of electrons, the maximum current obtained during the experiment, is $\sim$ 1700 sec (see Table II), and so the rate of depolarization of the ^{3}He nuclei in the target is roughly 1.6×10^{16}/sec. At this beam current, if the polarized ^{3}He remained in the beam path, they would depolarize in approximately 20 sec. However, the atoms diffuse out of the beam path in about 4 msec and to the walls within approximately 1 sec, and so the gas in the target cell is mixed on a time scale much shorter than the time for depolarization. During the experiment, the average beam current was 11 μA, and so the polarization in the beam path is estimated to have differed only by $\Delta P \sim 0.03P$ from the average polarization.

Tests to assess the depolarizing effects of an electron beam were performed using a beam of 250 MeV unpolarized electrons. Measurements to determine the ratio of the polarizations in the target and pumping cells, P_t/P_p, and the spin relaxation time constant in the target cell, τ_t, were made at beam currents of 5.6, 11, 22, 33, and 44 μA. Figure 8 shows the measured ratio as a function of the target cell relaxation time, which varies with the beam current. The solid curve is a calculation based upon the geometry of the system and the measured relaxation times. Table II summarizes the results, including the contribution to the relaxation time from beam effects, $\tau_{\rm beam}$, as a function of beam current. The beam-induced relaxation rate varies roughly linearly with the beam current. These results show that the polarized ^{3}He target operates without serious loss of polarization with 40 μA of minimum ionizing beam current.

During the experiment, the target polarization ranged between 18% and 32% with beam on target. Over the course of the experiment, the target performance varied, with a general decline in the polarization over a 2 month period. The polarization was higher at the beginning of the experiment than in the latter part of the run. There are several factors that contributed to the decline in the target performance. One is that the nitrogen coating on the foil windows was slowly evaporated by the beam, on the time scale of a few days. When the cell was recoated with frozen nitrogen, the target polarization improved markedly. In addition, during test runs of the Møller polarimeter, which were done before this experiment started but after the target was installed in the beam line, the target cell was heated by beam spray and contaminants were released into the cell, probably from the epoxy used to attach the foil windows. The contaminants destroy the metastable atoms, decreasing the optical pumping efficiency. Furthermore, exposure of the laser to dust caused a degradation of the performance and stability over time. These factors contributed to the lower average polarization achieved during the experiment, compared with the typical value of 30% obtained prior to the beginning of the experiment. With the knowledge gained during this experiment, more consistent operation of the polarized target is possible during future runs. The use of the higher-power LMA lasers, which are more stable than the YAP laser, have already improved the target performance. Subsequent to the experiment reported here, 50% polarization at $T = 12$ K has been achieved with this target without any changes

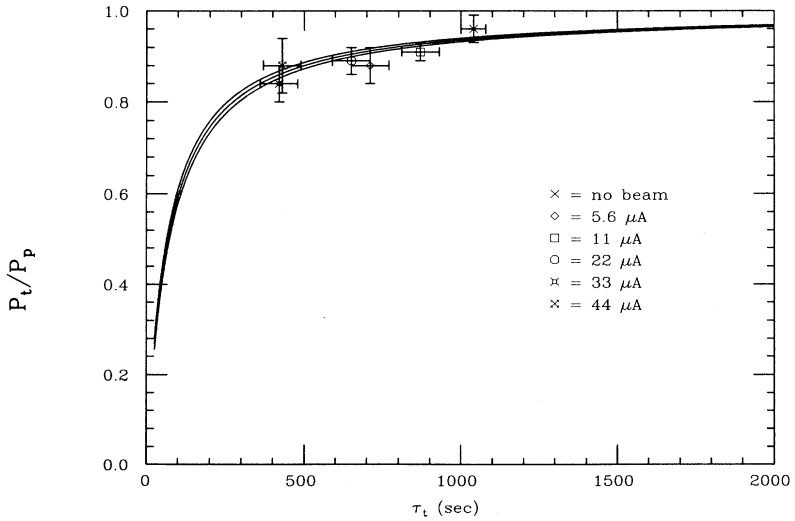

FIG. 8. Measured equilibrium ratio of the polarization in the target cell to the polarization in the pumping cell as a function of the relaxation time in the target cell. The curves are calculations using the cell geometry of the target system, assuming exchange times of $t_{ex} = 7.5 \pm 0.5$ sec. The beam currents at which the data were taken are indicated on the plot.

TABLE II. Target cell relaxation time constant τ_t and equilibrium polarization ratio vs beam current. P_t/P_p is the ratio of the polarization in the target cell to the polarization in the pumping cell after equilibrium has been reached during optical pumping. The contribution to the relaxation time from beam effects, τ_{beam}, is indicated.

I (μA)	P_t/P_p	τ_t (sec)	τ_{beam} (sec)
0	0.96 ± 0.03	1040 ± 40	
5.6	0.88 ± 0.04	710 ± 60	2200 ± 600
11	0.91 ± 0.02	870 ± 60	5300 ± 2500
22	0.89 ± 0.03	650 ± 60	1700 ± 400
33	0.85 ± 0.04	420 ± 60	700 ± 170
44	0.88 ± 0.06	430 ± 60	730 ± 180

to the system except the use of the LMA laser as the optical pumping light source [27].

V. DATA ANALYSIS

The data analysis for this experiment involved the extraction of the observed asymmetry in the cross section when the helicity of the incident electrons was reversed. The spin-dependent yield was calculated from events of each beam helicity, correcting for differences in charge, and accounting for yield from background sources such as scattering from the target walls, pion production, and events in the elastic radiative tail. The data were collected in runs lasting approximately 1 h each, and the asymmetries calculated for each run are normalized to 100% polarization using the average target and beam polarizations during the run. The beam polarization did not vary significantly on the time scale of individual runs, and the average beam polarization measured in four Møller runs spaced throughout the experiment is used as the normalization. Details of the Møller polarimeter and the beam polarization measurements are found in Ref. [12].

The extraction of the quasielastic asymmetry from the experimental spin-dependent cross sections involved a number of corrections. In general, the corrections can be split into two categories, those that arise from a dilution of the cross section from some background source and those that involve a spin-dependent asymmetry directly. Examples of the former type are the corrections for the empty target background, pion production, and the yield in the elastic radiative tail under the quasielastic peak. The correction for these effects is a renormalization of the asymmetry,

$$A_{\text{corrected}} = \frac{\sigma_{\text{total}}}{\sigma_{\text{total}} - \sigma_{\text{bkgrd}}} A_{\text{expt}}. \tag{15}$$

The other type of correction involves the subtraction of an asymmetry from the experimental value,

$$A_{\text{corrected}} = A_{\text{expt}} - \Delta A. \tag{16}$$

An example of this type of correction is the subtraction of the helicity-dependent asymmetry in the elastic radiative tail under the quasielastic peak.

The full expression used in this analysis to extract the ^{3}He quasielastic asymmetry from the experimental asymmetry is

$$A_{\text{QE}} = A_{\text{expt}} \left(\frac{1}{1 - d_{\text{empty}} - d_{\text{eltail}} - d_\pi} \right) - A_{\text{eltail}} \left(\frac{d_{\text{eltail}}}{1 - d_{\text{empty}} - d_{\text{eltail}} - d_\pi} \right) + \Delta A_{\text{rad}}, \tag{17}$$

where the dilution ratios d are defined as $d_{\text{bkgrd}} = \sigma_{\text{bkgrd}}/\sigma_{\text{total}}$. A_{eltail} is the asymmetry from elastic background events under the part of the quasielastic peak used for the analysis, and ΔA_{rad} is the quasielastic radiative correction to the asymmetry. In principle, there also may be an asymmetry in the pion background. However, since no experimental data exist for this, the pion asymmetry is assumed to be zero and a systematic uncertainty of $\pm 10\%$ in $\Delta A/A$ is included to reflect our lack of knowledge about its value.

In general, the corrections to the asymmetry are energy dependent. The corrections to the OHIPS data reported here are integrated over the spectrometer acceptance, as is the calculated asymmetry, because the statistics on the measurement are not sufficient to provide information about the energy dependence. The corrections to the asymmetry measured with BIGBITE were applied as a function of the energy transfer ω in the energy range accepted by the spectrometer, and the measured asymmetry as a function of ω is reported. The quasielastic analysis of the BIGBITE data was restricted to the energy region $58 \leq \omega \leq 161$ MeV to cut out the events in the tail of the peak where the asymmetry is dominated by the high-momentum components of the ^{3}He wave function. The asymmetry integrated over this kinematic region is also reported.

Table III contains the dilution ratios for the empty target background, the elastic radiative tail, and the pion background for both spectrometers. For the empty target runs, the ^{3}He gas was pumped out of the system, and so the geometry was exactly the same as with the target full. Figure 9 shows the empty and full target yields as a function of ω for the OHIPS and BIGBITE raw data. The yields are normalized to account for accumulated charge and detection efficiency differences between the empty and full target runs. The OHIPS yield includes only the central part of the quasielastic peak, while the BIGBITE spectrometer covers both the elas-

TABLE III. Fraction of the total yield in the quasielastic region attributable to different background sources. These numbers are used to correct the experimental asymmetry for the dilution of the quasielastic yield from other scattering processes.

Background source	OHIPS	BIGBITE
Empty target	0.096 ± 0.016	0.15 ± 0.04
Elastic radiative tail	0.011 ± 0.001	0.039 ± 0.004
Pion	0.011 ± 0.011	0.022 ± 0.022

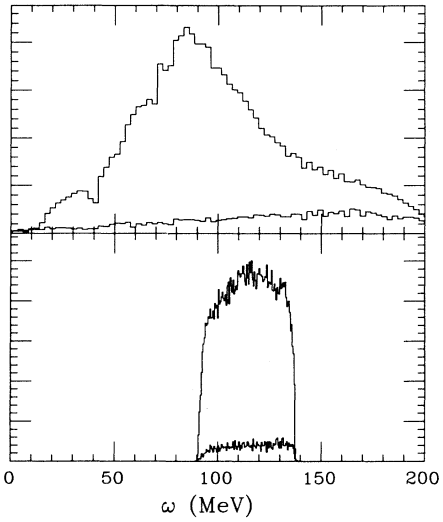

FIG. 9. Yield with the target cell empty vs with the target cell filled with $1.2 \times 10^{18}/\text{cm}^3$ ^{3}He atoms. The upper plot is the yield in the BIGBITE spectrometer, and the lower is the yield in the OHIPS spectrometer.

tic peak and a large part of the quasielastic peak. The events in the small peak centered around $\omega = 30$ MeV are the elastic events, smeared by the spectrometer resolution; as this spectrum shows, the momentum smearing in the BIGBITE spectrometer is quite substantial for an extended target. Because of the resolution, the elastic data cannot be separated from the low-ω events in the quasielastic peak. The elastic radiative tail was calculated for the kinematics of the two measurements using the procedure of Mo and Tsai [28]. The calculated yield for BIGBITE was smeared by the momentum resolution of the spectrometer to obtain a more realistic estimate of the elastic radiative tail contribution under the part of the quasielastic peak used to extract the asymmetry. The elastic yield is estimated to be 1.1% of the total yield in the OHIPS spectrometer and 3.9% of the yield in the portion of the BIGBITE spectra used for the data analysis. A fractional uncertainty of 10% is assigned to the estimated elastic yield. The contribution to the cross section from pion electroproduction was calculated taking into account the effect of Fermi motion by including the nucleon momentum in the scattering process and transforming from the nucleon rest frame to the laboratory frame to calculate the cross section. The results indicate that the pions contribute 1.1% of the total yield in the OHIPS spectrometer and 2.2% of the total yield in the energy region used for the quasielastic asymmetry analysis of the BIGBITE data. As was done for the elastic radiative tail, the pion yield for BIGBITE was smeared over the momentum acceptance of the spectrometer before integration. The fractional uncertainty assigned to the calculated pion yield is 100%.

For ^{3}He, the asymmetry in the elastic peak may be comparable to, or even exceed, the asymmetry in the quasielastic peak. Therefore, it is important to correct for the asymmetry in the elastic radiative tail under the part of the spectrum used to calculate the quasielastic asymmetry. For this correction, the elastic asymmetry was calculated from fits to the experimentally determined charge and magnetic form factors of ^{3}He [29], using the formalism of Donnelly and Raskin for inclusive scattering asymmetries [4]. If there is a spin-dependent asymmetry at the elastic peak, then there is also an asymmetry in the radiative tail, although the value may be different from the peak value because of the spread in energies of the incident and scattered particles contributing to the tail. To calculate the asymmetry of the elastic radiative tail, the spin-dependent elastic radiative cross section as a function of ω was calculated separately for left and right helicity electrons, following the procedure of Mo and Tsai. The elastic asymmetry used for the correction is the difference in the calculated spin-dependent cross sections, divided by the unpolarized cross section. At the kinematics of the OHIPS measurement, the contribution to the experimental asymmetry is negligible. The contribution to the BIGBITE experimental asymmetry, however, is substantial; the asymmetry ranged from 13.5% to 17.5% in the energy range used for the quasielastic analysis. A 10% fractional uncertainty is assigned to the calculated asymmetry in the elastic radiative tail.

In addition to the corrections discussed above, the quasielastic cross section extracted from the experimental data should be corrected for quasielastic radiative effects. Calculations of the helicity-dependent cross section for quasielastic scattering, from which the theoretical quasielastic asymmetry is obtained, assume single photon exchange in the scattering process. However, the measured cross section, and hence the asymmetry, includes effects from higher-order processes such as bremsstrahlung and energy straggling. Let σ_{rad} denote the quasielastic cross section including radiative effects, and σ denote the cross section one obtains assuming single photon exchange. In the limit where $A \ll 1$ and the radiative correction is small, the quasielastic asymmetry can be written as

$$A = A_{\text{rad}} + \Delta A_{\text{rad}}, \tag{18}$$

where the asymmetry correction is

$$\Delta A_{\text{rad}} \approx \frac{1}{2}\left(\frac{\sigma_+/\sigma_{\text{rad}+} - \sigma_-/\sigma_{\text{rad}-}}{\sigma_+/\sigma_{\text{rad}+}}\right). \tag{19}$$

For this analysis the correction factor was calculated using the procedure of Mo and Tsai for inelastic scattering and the model of the ^{3}He quasielastic asymmetry of Friar *et al.* [5]. The use of a more sophisticated calculation that includes the ω dependence of the asymmetry does not change the results reported here because of the small size of the correction. For the OHIPS data, the correction is $\Delta A_{\text{rad}} \approx 0.001$ and is the same for the two different target spin orientations. This is expected since the asymmetry is insensitive to small changes in Q^2 at kinematics where it is dominated by G_M^n. The correction to the BIGBITE data depends strongly upon the target spin direction because the asymmetry is more strongly dependent upon Q^2 at kinematics sensitive to

G_E^n. The correction was applied separately to the data for each spin direction and is small (~ 0.0005) in all cases. For the BIGBITE correction, ΔA_{rad} was smeared by the spectrometer resolution.

Helicity-correlated variations in beam, target, or detector properties give rise to false asymmetries. The data from each run were analyzed for variations of detector efficiencies for electrons detected during beam pulses of different helicities; the false asymmetry from this source is consistent with zero within the statistical uncertainty of the efficiency measurement. In addition, the false asymmetries from helicity-correlated variations in the electron beam energy and position were estimated.

Because of the energy dependence of the cross section, shifts in the beam energy correlated with the electron helicity appear as false asymmetries in the data. If beam pulses of different helicity carry slightly different amounts of charge, then this type of false asymmetry can arise from beam loading, the phenomenon where the beam energy varies with the intensity of the beam pulse. For this experiment, the contribution from beam loading is negligible; the estimated false asymmetry is approximately three orders of magnitude smaller than the measured asymmetry.

A helicity-correlated beam position shift can give rise to a false asymmetry if there is a position dependence to the background rates from the empty target. The beam position was measured for each beam pulse using an rf cavity beam position monitor, and the helicity-correlated beam position shift was calculated for each run using the information. Although no evidence of a helicity-correlated beam position shift in the x direction (horizontal) was seen, a statistically significant shift of 4 μm in the y direction (vertical) was observed. The shift could have been caused by the x-y coupling in the accelerator magnetic optics or by variations in the polarized electron source [11]. The systematic error in the quasielastic asymmetry from a false asymmetry arising from the helicity-correlated beam shift was calculated from runs taken with the beam at different positions in the empty target cell and found to contribute an uncertainty of 0.01 to $\Delta A/A$.

VI. RESULTS

The OHIPS asymmetry was calculated from the events within the energy acceptance of the spectrometer, $90 \leq \omega \leq 138$ MeV. Table IV shows the results for the data taken with different target spin orientations and for the sum of all the data. The delivered beam charge and average target polarization for each data set are also indicated in the table. The results for the individual data sets are consistent, and the asymmetry changes sign when the direction of the nuclear spin is reversed.

Table V shows the individual contributions to the systematic uncertainty for the OHIPS measurement from the various error sources. The dominant sources of uncertainty are the target and beam polarizations and the asymmetry in the pion background. The systematic precision could be improved in future measurements by using a Čerenkov detector to distinguish electrons from pions. The Møller polarimeter used in this experiment was newly installed in the beam line and thorough testing of the apparatus was not completed before this experiment ran. The beam polarimetry can be improved through more detailed studies of the systematic errors in the device. The systematic uncertainties associated with the target come from the empty target background and the precision of the polarization measurement. The background from the target cell walls is small enough that this is not a significant source of systematic error. The target polarimetry can be improved to the level of $\sim 5\%$ systematic precision using the new information from NMR calibrations of the optical polarization and more sophisticated techniques in optical polarimetry [23].

In Table IV, calculations of the quasielastic asymmetry are shown for comparison with the OHIPS experimental result. The measured asymmetry is consistent with the theoretical models of Blankleider and Woloshyn [1], Ciofi degli Atti *et al.* [7], and Friar *et al* [5]. The Blankleider-Woloshyn calculation uses the dipole form for the proton form factors and the neutron magnetic form factor, and the Galster parametrization of the neutron electric form factor [30], $G_E^n(Q^2) = -\tau G_M^n/(1+5.6\tau)$. The calculation of Ciofi degli Atti, Pace, and Salmè shown in Table IV uses the Gari-Krümpelmann form factors [31]. Figure 10 shows the ω dependence of the quasielastic asymmetry at the kinematics of the OHIPS measurement, calculated with the model of Blankleider and Woloshyn. The contributions from the protons and neutrons are indicated on the plot. The asymmetry is reasonably flat, and the neutron contribution dominates in the region within the spectrometer acceptance. Analysis using the model of

TABLE IV. Results of the OHIPS asymmetry measurement for each of the target spin orientations and for the combined data set. The asymmetry error specified for the individual data sets is statistical only, while the two errors on the final result are statistical and systematic, respectively. The amount of charge in each set and the average target polarization for the ^{3}He runs are also indicated. The predictions of the models of Blankleider and Woloshyn (A_{BW}), Ciofi degli Atti *et al.* (A_{C}), and Friar *et al.* (A_{F}) are shown for comparison with the measured asymmetries.

β	θ^*	ϕ^*	charge (μA h)	$< P_t >$ (%)	A_{QE} (%)	A_{C} (%)	A_{BW} (%)	A_{F} (%)
$-51.5°$	$0.9°$	$0°$	239	26.6	-3.8 ± 3.0		-4.7	-4.4
$-44.5°$	$7.9°$	$0°$	333	22.0	-2.5 ± 2.9		-4.5	-4.1
$135.5°$	$172.1°$	$180°$	808	21.5	$+4.4 \pm 2.8$		$+4.5$	$+4.1$
	Combined		1381	22.5	$-3.79 \pm 1.37 \pm 0.67$	-4.1	-4.5	-4.2

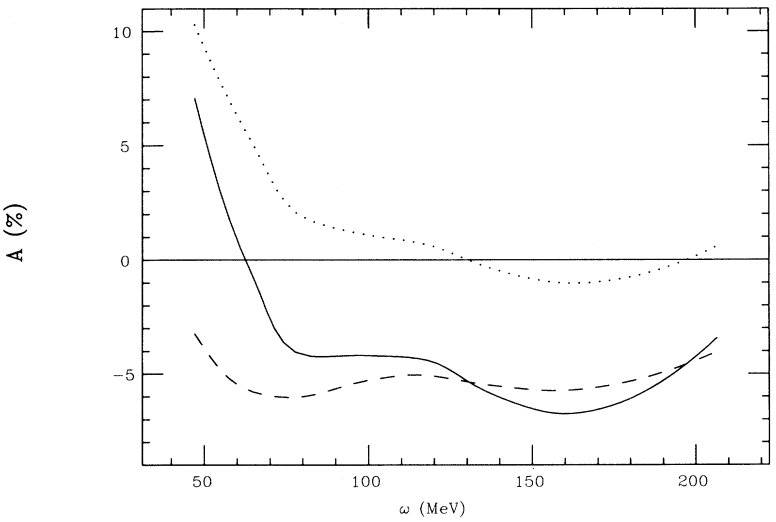

FIG. 10. Theoretical quasielastic asymmetry (solid line) as a function of energy transfer for the OHIPS kinematics, averaged over the spin orientations used for the OHIPS measurement, calculated using the formalism of Blankleider and Woloshyn. The contributions from the protons (dots) and the neutron (dashes) are shown. The energy range $90 \leq \omega \leq 138$ MeV is used to calculate the quasielastic asymmetry from the experimental data.

Friar *et al.* indicates that the fractional uncertainty in the theoretical asymmetry, $\frac{\Delta A}{A}$, from nuclear structure effects is 4%.

The statistics of the BIGBITE measurement are sufficient for the measured asymmetry to be binned as a function of ω for comparison with theoretical predictions of the energy dependence. Figure 11 shows the measured asymmetry for $58 \leq \omega \leq 161$ MeV . The error bars on the data include only the statistical uncertainty. The values of the quasielastic asymmetry as a function of ω are tabulated in Table VI. The asymmetry results, integrated over the energy region $58 \leq \omega \leq 161$ MeV, are given in Table VII, along with calculations following Blankleider and Woloshyn, those of Ciofi degli Atti *et al.*, and the model of Friar *et al.* The experimental data agree well with the calculations. The individual contributions to the systematic uncertainty are shown in Table VIII.

Although the BIGBITE measurement depends primarily upon the interference response function $R_{TL'}$, because the target spin was not oriented at 90° to the **q** direction, there is a contribution to the cross section from $R_{T'}$. Furthermore, since the neutron electric form factor is relatively small for $Q^2 = 0.16$ $(\mathrm{GeV}/c)^2$ compared with the proton electric form factor, the contribution from the proton to the interference term is significant. Figure 11 shows the energy dependence of the measured quasielastic asymmetry compared with the Blankleider-Woloshyn calculation. The contributions of the protons and neutron are indicated on the plot. The calculation indicates that the asymmetry is reasonably flat in the region used for the extraction of the quasielastic asymmetry, and that even though the neutron contribution dominates, the protons contribute significantly to the asymmetry. The estimated uncertainty from nuclear structure effects in the calculated ^{3}He quasielastic asymmetry is $\frac{\Delta A}{A} = 13\%$.

Since the momentum acceptance of BIGBITE is $\Delta p/p \sim \pm 25\%$, quasielastic and elastic events were collected simultaneously. However, because of the poor momentum resolution for an extended target, it is impossible to separate the events in the elastic peak, centered at $\omega \sim 30$ MeV, from events near the inelastic two- and three-body thresholds at 5.5 and 7.7 MeV above the elastic peak, respectively. The asymmetry measured in the region $11 \leq \omega \leq 37$ MeV is $+25 \pm 5\%$ (statistical errors only). Systematic errors are estimated to be $\pm 8\%$. The measured value is consistent with the theoretical elastic asymmetry of 18%, but for this measurement the statistics and the spectrometer resolution were not sufficient for the elastic asymmetry to be useful as a polarization monitor.

Another experiment that measured the quasielastic

TABLE V. Contributions to the systematic uncertainty in the OHIPS quasielastic asymmetry from the individual error sources.

Systematic uncertainty	$\frac{\Delta A}{A}$
Beam polarization	0.105
Target polarization	0.100
Empty target subtraction	0.018
Elastic radiative corrections	0.001
Quasielastic radiative corrections	0.008
Pion cross section	0.012
Pion asymmetry	0.100
Helicity-correlated efficiency variations	0.012
Helicity-correlated beam shifts	0.010
total	0.177

TABLE VI. Measured quasielastic asymmetry as a function of ω for $E = 574$ MeV and $\theta = 44.0°$. The error bars reflect the statistical uncertainty only. The systematic uncertainty $\frac{\Delta A}{A} = 0.21$ is nearly independent of the energy transfer in this energy range.

ω	A_{QE}
68.8	4.8 ± 2.6
88.3	1.3 ± 2.2
108.3	-0.3 ± 2.7
128.9	5.2 ± 3.8
149.9	4.5 ± 5.3

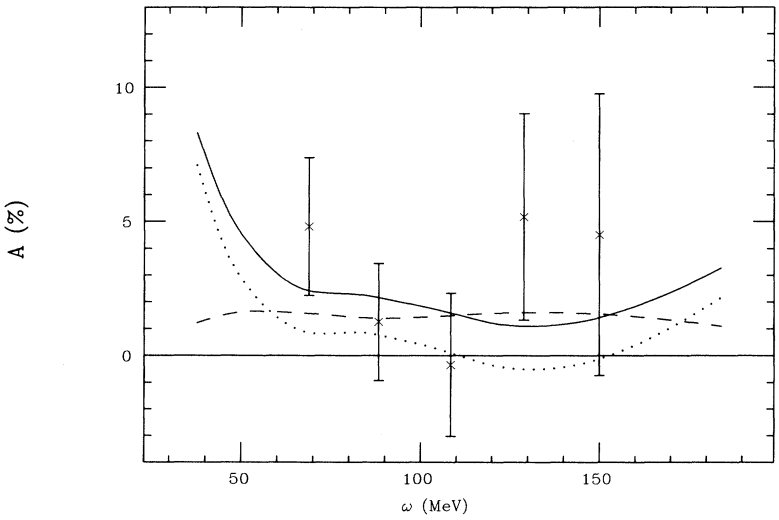

FIG. 11. Theoretical quasielastic asymmetry (solid line) as a function of energy transfer for the BIGBITE kinematics, averaged over the spin orientations used for the measurements, calculated using the formalism of Blankleider and Woloshyn. The calculated contributions from the protons (dots) and the neutron (dashes) are shown. The measured quasielastic asymmetry in the energy range $58 \leq \omega \leq 161$ MeV is also plotted. The error bars reflect the statistical uncertainty only.

^{3}He asymmetry [32], also performed using the MIT-Bates accelerator, obtained results consistent with ours. The experiment was similar to the one described here with the exception that a different polarized ^{3}He target was employed. The target used spin exchange between ^{3}He and optically pumped Rb vapor as the polarization technique [33]. The asymmetries proportional to $R_{TL'}$ and $R_{T'}$ were measured at $Q^2 = 0.20$ (GeV/c)^2. Figure 12 shows the results from both experiments and the predictions of Blankleider and Woloshyn and of Ciofi degli Atti *et al.* The differences in the theoretical predictions of $A_{T'}$ for the measurements of the two experiments, which were both made at $Q^2 = 0.20$ (GeV/c)^2, arise because the ^{3}He spin directions were slightly different in the two experiments. There is good agreement of both $A_{T'}$ and $A_{TL'}$ with the predictions of the plane wave impulse approximation within the precision of the experimental data.

VII. CONCLUSIONS

The experiment reported in this paper used a new type of polarized target for electron scattering experiments, which employs laser optical pumping in a small magnetic holding field to orient the nuclei. The information on the target presented here shows that laser-driven metastability exchange polarized ^{3}He targets can operate in the high-beam-current environments encountered at electron accelerators. Since studies of polarized ^{3}He have been suggested as a way to obtain information about the electromagnetic properties of the neutron, quasielastic asymmetry measurements, such as this one, are important in assessing how well the ^{3}He nuclear structure effects are understood. The results of this experiment show that the metastability exchange polarized ^{3}He target has relatively little background from impurities or from scattering from the target walls, making it a clean tool for quasielastic studies.

The experimental data support the assertion that polarized ^{3}He can be used to study the neutron. Although the results agree with predictions using the plane wave impulse approximation and realistic ^{3}He wave functions, clearly experimental data of better precision are needed. To this end, both statistical and systematic precision must be improved. Theoretical calculations including final state interactions and meson exchange currents in spin-dependent scattering also are needed to study the reaction mechanism. Exclusive scattering experiments can provide information about the small components of the ^{3}He wave function needed for the extraction of nucleon and quark properties from polarized ^{3}He data.

ACKNOWLEDGMENTS

We would like to thank B. Blankleider and R. Woloshyn for providing us with their computer code. We also thank T. Gentile and H. Gao for their help with the analysis. The research was supported by the National Science Foundation Grant No. PHY88-17296 (Caltech)

TABLE VII. Results of the BIGBITE quasielastic asymmetry measurement for each of the target spin orientations and for the combined data set. The data are integrated over the energy range $58 \leq \omega \leq 161$ MeV. The notation is the same as in Table IV.

β	θ^*	ϕ^*	charge (μA h)	P_t (%)	A_{QE} (%)	A_C (%)	A_{BW} (%)	A_F
−51.5°	108.4°	0°	228	26.6	$+3.2 \pm 2.7$		+2.3	+2.5
−44.5°	101.4°	0°	336	22.0	$+2.9 \pm 2.7$		+1.9	+2.1
135.5°	78.6°	180°	808	21.5	-1.9 ± 1.7		−1.9	−2.1
	Combined		1372	22.5	$+2.41 \pm 1.29 \pm 0.51$	+2.7	+2.0	+2.2

TABLE VIII. Contributions to the systematic uncertainty in the BIGBITE quasielastic asymmetry from the individual error sources.

Systematic uncertainty	$\frac{\Delta A}{A}$
Beam polarization	0.105
Target polarization	0.100
Empty target subtraction	0.050
Elastic radiative corrections	0.046
Quasielastic radiative corrections	0.012
Pion cross section	0.021
Pion asymmetry	0.100
Helicity-correlated efficiency variations	0.090
Helicity-correlated beam shifts	0.010
total	0.212

and by the U.S. Department of Energy Contract No. DE-AC02-76ER03069 (MIT).

APPENDIX: RELAXATION AND PUMPING RATE EQUATIONS FOR A DOUBLE-CELL POLARIZED TARGET SYSTEM

To extract the asymmetry from the measured cross section, it is necessary to know the nuclear polarization of the ^{3}He in the target cell. In a double-cell system with the cells in diffusive contact so that the atoms pass back and forth between the two volumes, the target cell

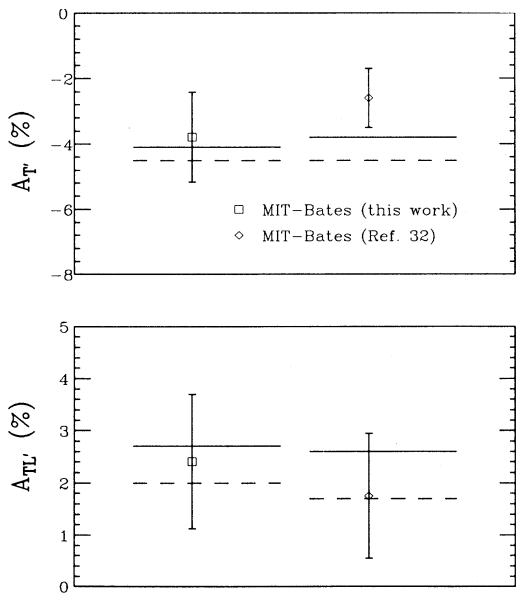

FIG. 12. Comparison of the world's data on the $^3\overrightarrow{\text{He}}(\vec{e},e')$ quasielastic asymmetry with calculations using the formalism of Blankleider and Woloshyn (dashed line) and with predictions of Ciofi degli Atti *et al.* (solid line). $A_{T'}$ is sensitive to $R_{T'}$, and $A_{TL'}$ is sensitive to $R_{TL'}$. The measurements of Ref. [32] are made at $Q^2 = 0.20$ (GeV/c)^2, and the data of this work are at $Q^2 = 0.20$ (GeV/c)^2 ($A_{T'}$) and at $Q^2 = 0.16$ (GeV/c)^2 ($A_{TL'}$). The errors bars on the experimental data include only the statistical uncertainty.

polarization can be determined indirectly from the polarization of the atoms in the pumping cell, which can be monitored continuously with an optical polarimeter that measures the circular polarization of the $3^1D_2 \rightarrow 3^1P_1$ emission line from 3^1D_2 excited state atoms created by the discharge. One can infer the polarization of the target cell atoms from the measured polarization of the pumping cell population and some additional information about the coupling of the two cells, such as the fraction of ^{3}He in each cell, the polarization relaxation time of the system, and the characteristic time for the exchange of atoms between the cells. The volumes and temperatures of the two cells and the pressure provide the information about the fraction of atoms in each cell, and measurements of the polarization relaxation are used to determine the time constants of the system. In this appendix, the relationships needed to extract the time constants and the target polarization from measurements of the polarization in the pumping cell during spin relaxation are presented. Data taken with the polarized ^{3}He target and used to determine the target polarization are shown. In addition, the equations governing the polarizations achievable in the system during optical pumping are presented. These relationships are useful in the design of a polarized target system because they yield predictions of the achievable polarization in the target cell for given optical pumping rates and relaxation times.

Equations describing the time evolution of the polarizations in both cells of a coupled two-cell system can be obtained from the solutions to the rate equations for the polarization in the cells. In the discussion that follows a design such as the one used for the Caltech polarized ^{3}He target is assumed: The atoms are optically pumped in one cell, referred to as the pumping cell, and are in diffusive contact with a second cell, referred to as the target cell. The equations assume that the transfer tube has negligible volume and that there is no time lag between when the atoms leave one cell and enter the other. Since the polarization evolves on the time scale of seconds, which is much longer than the time spent in the transfer tube, the delay in transferring between the cells can be ignored.

1. Solution to spin relaxation rate equations

The spin relaxation rate equations for the polarization in each cell of a double-cell system are

$$\dot{P}_p(t) = -\frac{P_p(t)}{\tau_p} + \frac{P_t(t) - P_p(t)}{t_p} \tag{A1}$$

and

$$\dot{P}_t(t) = -\frac{P_t(t)}{\tau_t} + \frac{P_p(t) - P_t(t)}{t_t}, \tag{A2}$$

where the first term on the right-hand side accounts for the spin relaxation in the cell and the second accounts for the exchange of polarization between the two cells. The quantities entering the equations are the pumping and target cell polarizations $P_p(t)$ and $P_t(t)$, the relaxation time in the pumping and target cells, τ_p and τ_t, and the

exchange time for the pumping and target cell populations, t_p and t_t. First, consider the exchange terms in Eqs. (A1) and (A2). Atoms diffuse out of the pumping cell carrying polarization away from the cell at a rate $\frac{1}{t_p}$ and out of the target cell carrying polarization away at a rate $\frac{1}{t_t}$. However, the polarization is defined in terms of the number of atoms in the cell from which the atoms diffuse,

$$P \equiv \frac{N_+ - N_-}{N_+ + N_-}, \tag{A3}$$

and must be corrected by the number of atoms in the cell which they enter in order to reflect correctly the amount of polarization contributed. For a closed system detailed balance requires that the number of atoms leaving one cell equal the number of atoms entering the other to maintain a constant pressure, i.e.,

$$\frac{N_p}{t_p} = \frac{N_t}{t_t}. \tag{A4}$$

In addition, the exchange rate that one measures is the sum of the rates from the two cells,

$$\frac{1}{t_{\text{ex}}} = \frac{1}{t_p} + \frac{1}{t_t}. \tag{A5}$$

Using Eqs. (A4) and (A5), the relaxation rate equations can be rewritten in matrix form as

$$\begin{pmatrix} \dot{P}_p(t) \\ \dot{P}_t(t) \end{pmatrix} = \begin{pmatrix} -\left(\frac{1}{\tau_p} + \left(\frac{N_t}{N}\right)\frac{1}{t_{\text{ex}}}\right) & \left(\frac{N_t}{N}\right)\frac{1}{t_{\text{ex}}} \\ \left(\frac{N_p}{N}\right)\frac{1}{t_{\text{ex}}} & -\left(\frac{1}{\tau_t} + \left(\frac{N_p}{N}\right)\frac{1}{t_{\text{ex}}}\right) \end{pmatrix} \begin{pmatrix} P_p(t) \\ P_t(t) \end{pmatrix}. \tag{A6}$$

The solutions for the polarizations during relaxation display double-exponential decay. The time evolution of the polarizations of the pumping and target populations, written as a sum of two exponentials with two new time constants τ_s and τ_l, is

$$\begin{pmatrix} P_p(t) \\ P_t(t) \end{pmatrix} = \frac{1}{\Delta\alpha} \begin{pmatrix} [\alpha_+ P_p(0) - P_t(0)]e^{-t/\tau_s} + [P_t(0) - \alpha_- P_p(0)]e^{-t/\tau_l} \\ \alpha_-[\alpha_+ P_p(0) - P_t(0)]e^{-t/\tau_s} + \alpha_+[P_t(0) - \alpha_- P_p(0)]e^{-t/\tau_l} \end{pmatrix}, \tag{A7}$$

where

$$\alpha_+ = \frac{\frac{1}{\tau_p} + \frac{1}{t_{\text{ex}}} - \frac{1}{\tau_l}}{\frac{1}{\tau_t} + \frac{1}{t_{\text{ex}}} - \frac{1}{\tau_l}} \tag{A8}$$

and

$$\alpha_- = \frac{\frac{1}{\tau_p} + \frac{1}{t_{\text{ex}}} - \frac{1}{\tau_s}}{\frac{1}{\tau_t} + \frac{1}{t_{\text{ex}}} - \frac{1}{\tau_s}}. \tag{A9}$$

From these relations, the polarizations in the two cells as a function of time during relaxation can be calculated exactly, assuming that the initial polarizations and time constants are known.

In practice, one may not initially know the time constants of the system, τ_p, τ_t, and t_{ex}. In this case, the pumping cell polarization can be measured as a function of time during the polarization relaxation process, and information about the time constants and the target polarization can be inferred from a fit of a sum of two exponentials to the data. The four-parameter fit has two time constants and two amplitudes multiplying the exponentials,

$$P_p(t) = a_s e^{-t/\tau_s} + a_l e^{-t/\tau_l}. \tag{A10}$$

From the time constants of the fit, τ_l and τ_s, information can be extracted about the time constants of the system, τ_p, τ_t, and t_{ex}. The relationships between the fit time constants and the time constants of the system are

$$\frac{1}{\tau_s} = \frac{1}{2}\left(\frac{1}{\tau_p} + \frac{1}{\tau_t} + \frac{1}{t_{\text{ex}}}\right) + \frac{1}{2}\sqrt{\frac{1}{t_{\text{ex}}^2} + \left(\frac{1}{\tau_p} - \frac{1}{\tau_t}\right)^2 + \frac{2}{t_{\text{ex}}}\left(\frac{N_t - N_p}{N}\right)\left(\frac{1}{\tau_p} - \frac{1}{\tau_t}\right)} \tag{A11}$$

and

$$\frac{1}{\tau_l} = \frac{1}{2}\left(\frac{1}{\tau_p} + \frac{1}{\tau_t} + \frac{1}{t_{\text{ex}}}\right) - \frac{1}{2}\sqrt{\frac{1}{t_{\text{ex}}^2} + \left(\frac{1}{\tau_p} - \frac{1}{\tau_t}\right)^2 + \frac{2}{t_{\text{ex}}}\left(\frac{N_t - N_p}{N}\right)\left(\frac{1}{\tau_p} - \frac{1}{\tau_t}\right)}. \tag{A12}$$

From these relationships, the exact expression

$$\frac{1}{\tau_s} + \frac{1}{\tau_l} = \frac{1}{t_{\text{ex}}} + \frac{1}{\tau_p} + \frac{1}{\tau_t} \tag{A13}$$

can easily be obtained. In the case where the exchange time is much shorter than the relaxation time in either cell, the short-time constant τ_s approximates the exchange time. Under these conditions, an approximate

expression for the long-time constant τ_l can be derived that depends only upon the relaxation times and the fraction of atoms in each cell:

$$\frac{1}{\tau_l} \approx \left(\frac{N_p}{N}\right)\frac{1}{\tau_p} + \left(\frac{N_t}{N}\right)\frac{1}{\tau_t}. \tag{A14}$$

This expression indicates that, in the limit of fast transfer between the cells, the rate of decay of the combined system is the average of the decay rates in each cell weighted by the number of atoms in the cell.

An important quantity to measure is the ratio of polarizations in the two cells just after the pumping light is shuttered for a relaxation measurement, $P_t(0)/P_p(0)$. If the relaxation measurement is started after equilibrium has been reached, then this ratio is the equilibrium polarization ratio attained in the system during optical pumping. Once this ratio is known, during optical pumping the target cell polarization can be inferred from measurements of the polarization in the pumping cell, which can be continuously monitored. The polarization in the pumping cell, $P_p(0)$, is measured directly, and the initial polarization in the target cell, $P_t(0)$, can be obtained from the amplitudes of the double exponential fit to the relaxation data using Eq. (A7).

Three types of measurements were made to determine the relaxation times of the polarized ^{3}He system: the relaxation time in the absence of the discharge that produces the metastable ^{3}He that are optically pumped and the relaxation time in the presence of the discharge both with and without depolarizing the nuclei in the pumping cell before beginning the measurement. The information from the three types of measurements provides redundancy in the extracted time constants and polarizations. Figure 13 shows an example of the measurement of the pumping cell polarization with the discharge on, along with the double-exponential fit to the decay. This measurement is made by shuttering the laser light and measuring the polarization in the pumping cell as a function of time. The measurement shown in Fig. 14 is similar to the one above, but in this case the polarization in the pumping cell is destroyed at the same time as the laser is shuttered. The polarization is destroyed by applying a small transverse field at the Larmor frequency to coils surrounding the pumping cell for a short time. This type of measurement gives a dramatic display of the polarization in the target cell as the polarized atoms from the target cell transfer into the pumping cell, building up the polarization. It also shows the rapid transfer between the two cells. Both measurements were made with 20 μA beam current on the target and show that polarizations of 30% can be maintained in the presence of beam.

2. Solution to optical pumping rate equations

For a single cell, the rate equation describing the polarization evolution during optical pumping is

$$\dot{P} = \frac{P_0 - P(t)}{T} - \frac{P(t)}{\tau_p}, \tag{A15}$$

where the first term reflects the pumping and the second term the relaxation. P_0 is the polarization achievable in the limit of no spin relaxation. The solution to this equation is

$$P(t) = \frac{P_0}{1+\frac{T}{\tau_p}}\left(1 - e^{-t\left(\frac{1}{T}+\frac{1}{\tau_p}\right)}\right). \tag{A16}$$

The achievable polarization in a single cell after pumping infinitely long,

$$P_s \equiv \frac{P_0}{1+\frac{T}{\tau_p}}, \tag{A17}$$

decreases with increasing relaxation time for a given pumping time constant T. The rate equation for a single cell can be rewritten in terms of P_s as

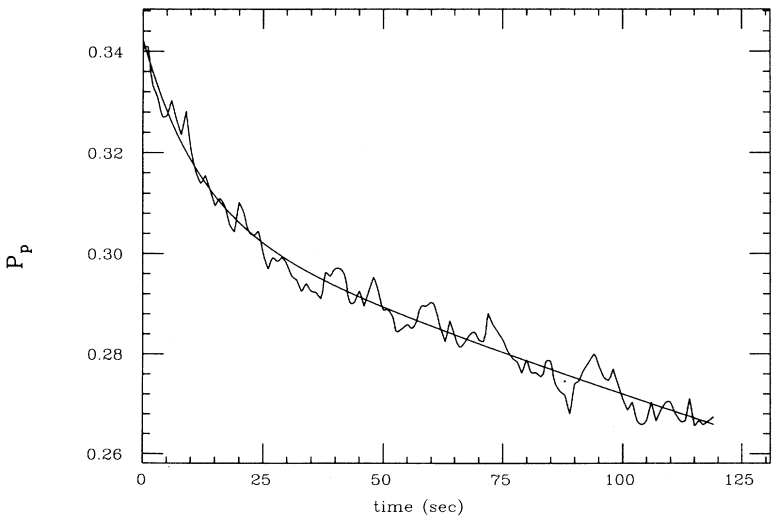

FIG. 13. Measurement of the pumping cell polarization relaxation. At time $t = 0$ the optical pumping light is shuttered, and the pumping cell polarization is measured as it decays. The smooth curve is a four-parameter fit to a sum of two exponentials. The data were taken with 20 μA of minimum ionizing beam current on target.

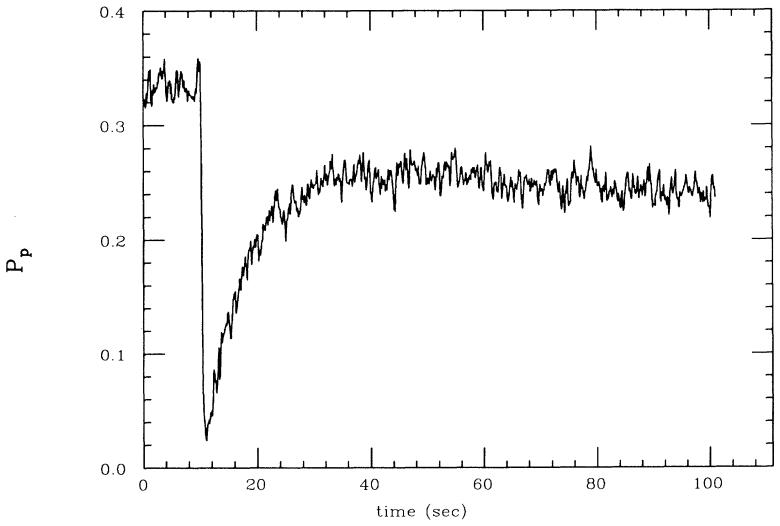

FIG. 14. Measurement of the pumping cell polarization during relaxation, with the polarization in the cell zeroed at time t = 10 sec. The repolarization is from polarized atoms transferring into the pumping cell from the target cell. The data were taken with 20 μA of minimum ionizing beam current on target.

$$\dot{P} = \left(\frac{1}{T} + \frac{1}{\tau_p}\right)[P_s - P(t)]. \tag{A18}$$

For the polarized ^{3}He target system optically pumped by light from a YAP laser, the pumping time constant was 20 – 30 sec.

For a coupled two-cell system where only one cell is optically pumped, the coupled rate equations for optical pumping are

$$\begin{pmatrix}\dot{P}_p(t)\\ \dot{P}_t(t)\end{pmatrix} = \begin{pmatrix}\left(\frac{1}{T}+\frac{1}{\tau_p}\right)P_s\\ 0\end{pmatrix} + \begin{pmatrix}-\left(\frac{1}{T}+\frac{1}{\tau_p}+\left(\frac{N_t}{N}\right)\frac{1}{t_{ex}}\right) & \left(\frac{N_t}{N}\right)\frac{1}{t_{ex}}\\ \left(\frac{N_p}{N}\right)\frac{1}{t_{ex}} & -\left(\frac{1}{\tau_t}+\left(\frac{N_p}{N}\right)\frac{1}{t_{ex}}\right)\end{pmatrix}\begin{pmatrix}P_p(t)\\ P_t(t)\end{pmatrix}, \tag{A19}$$

where P_s is the polarization achievable in a single cell of the same size as the pumping cell with pumping time constant T and relaxation time τ_p.

The pumping and target cell polarizations can be written in terms of two new time constants τ_l and τ_s as

$$\begin{pmatrix}P_p(t)\\ P_t(t)\end{pmatrix} = \frac{P_s}{\alpha_+ - \alpha_-}\left(\frac{1}{T}+\frac{1}{\tau_p}\right)\begin{pmatrix}(\alpha_+\tau_s - \alpha_-\tau_l) + \alpha_-\tau_l e^{-t/\tau_l} - \alpha_+\tau_s e^{-t/\tau_s}\\ \alpha_+\alpha_-\left[(\tau_s-\tau_l) + \tau_l e^{-t/\tau_l} - \tau_s e^{-t/\tau_s}\right]\end{pmatrix}, \tag{A20}$$

where

$$\alpha_+ = \frac{\frac{1}{T}+\frac{1}{\tau_p}+\frac{1}{t_{ex}}-\frac{1}{\tau_l}}{\frac{1}{\tau_t}+\frac{1}{t_{ex}}-\frac{1}{\tau_l}} \tag{A21}$$

and

$$\alpha_- = \frac{\frac{1}{T}+\frac{1}{\tau_p}+\frac{1}{t_{ex}}-\frac{1}{\tau_s}}{\frac{1}{\tau_t}+\frac{1}{t_{ex}}-\frac{1}{\tau_s}}. \tag{A22}$$

The exact relationship between the fit time constants of the pumping cell polarization data and the time constants of the system is

$$\frac{1}{\tau_s}+\frac{1}{\tau_l} = \frac{1}{T}+\frac{1}{\tau_p}+\frac{1}{\tau_t}+\frac{1}{t_{ex}}. \tag{A23}$$

The relationships between the fit time constants and the time constants of the system are

$$\frac{1}{\tau_l} = \frac{1}{2}\left(\frac{1}{T}+\frac{1}{\tau_p}+\frac{1}{\tau_t}+\frac{1}{t_{ex}}\right) - \frac{1}{2}\sqrt{\frac{1}{t_{ex}^2}+\left(\frac{1}{T}+\frac{1}{\tau_p}-\frac{1}{\tau_t}\right)^2+\frac{2}{t_{ex}}\left(\frac{N_t-N_p}{N}\right)\left(\frac{1}{T}+\frac{1}{\tau_p}-\frac{1}{\tau_t}\right)} \tag{A24}$$

and

$$\frac{1}{\tau_s} = \frac{1}{2}\left(\frac{1}{T}+\frac{1}{\tau_p}+\frac{1}{\tau_t}+\frac{1}{t_{ex}}\right) + \frac{1}{2}\sqrt{\frac{1}{t_{ex}^2}+\left(\frac{1}{T}+\frac{1}{\tau_p}-\frac{1}{\tau_t}\right)^2+\frac{2}{t_{ex}}\left(\frac{N_t-N_p}{N}\right)\left(\frac{1}{T}+\frac{1}{\tau_p}-\frac{1}{\tau_t}\right)}. \tag{A25}$$

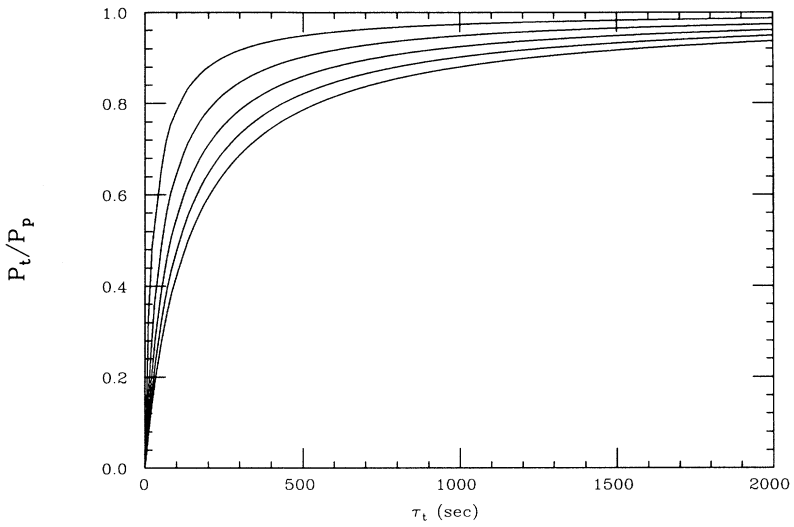

FIG. 15. Equilibrium ratio of target cell polarization to pumping cell polarization during optical pumping as a function of the relaxation time in the target cell, for different exchange times between the two cells. For the calculation $\tau_p = 200$ sec, $T = 25$ sec, and $\frac{N_t}{N} = 0.89$. The curves are for exchange times of 3, 6, 9, 12, and 15 sec. The ratio increases as the exchange time decreases.

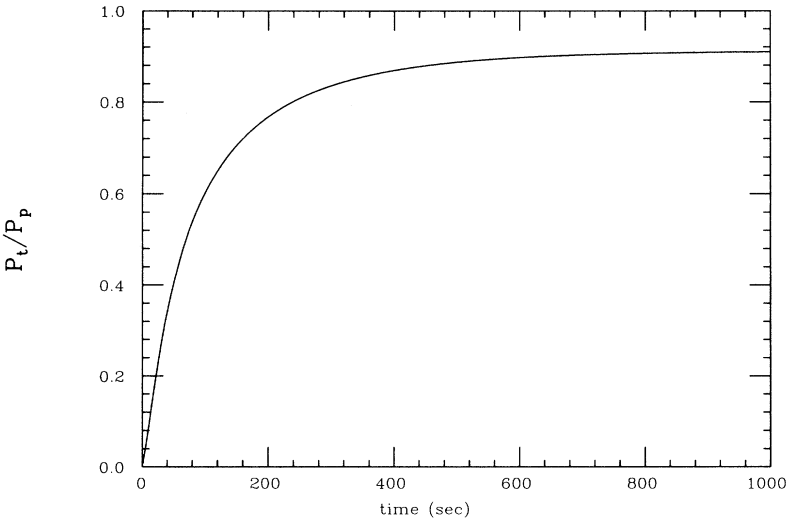

FIG. 16. Ratio of polarizations in the two cells, plotted as a function of time during optical pumping to show the approach to equilibrium of the polarizations. For the calculation $\tau_t = 700$ sec, $\tau_p = 200$ sec, $\tau_{ex} = 7.5$ sec, $T = 25$ sec, and $\frac{N_t}{N} = 0.89$. In this case, the system has reached equilibrium after approximately 800 sec.

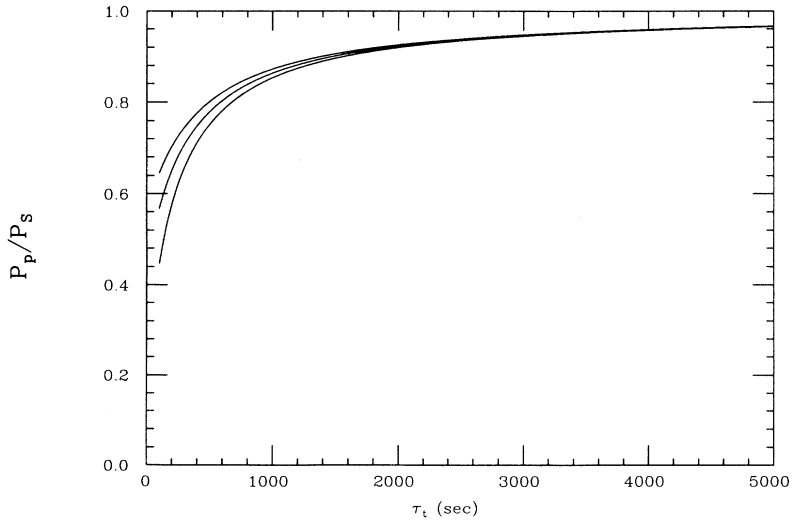

FIG. 17. Ratio of the equilibrium pumping cell polarization to the polarization attainable with a single cell of the same size as a function of the target cell relaxation time, for exchange times of 5, 15, and 25 sec. The ratio is smaller for shorter exchange times.

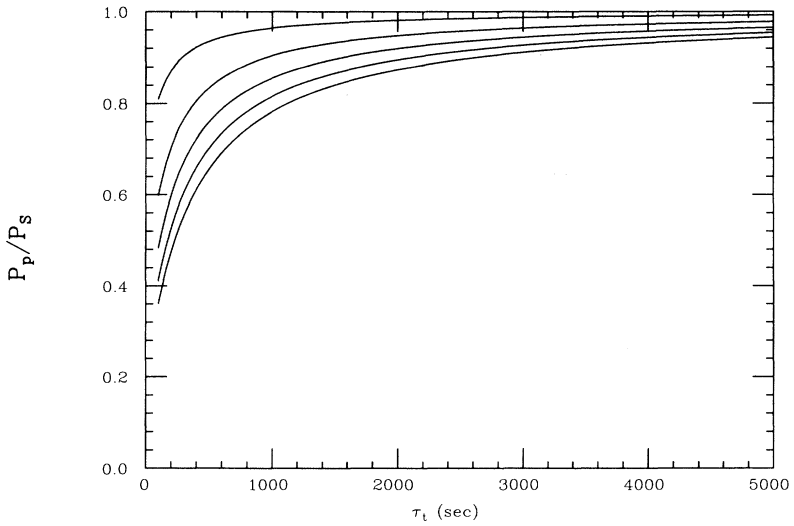

FIG. 18. Ratio of the equilibrium pumping cell polarization to the polarization attainable with a single cell of the same size, as a function of the target cell relaxation time, for pumping times of 5, 15, 25, 35, and 45 sec. The ratio is larger for shorter pumping times.

The expressions above give the general solution for the time evolution of the polarizations during optical pumping. For a closed system it is possible to use the pumping cell polarization as a monitor of the polarization in the target cell, the relevant volume for a scattering experiment. In this case, we are most interested in determining the equilibrium polarization ratio between the two cells, reached after the system has been optically pumped for awhile. The solution to this is much simpler than the full solution since it requires only that Eq. (A19) be zero. The equilibrium ratio of the target to pumping cell polarizations is

$$\frac{P_t}{P_p} = \frac{1}{1+\left(\frac{N}{N_p}\right)\frac{t_{ex}}{\tau_t}}. \tag{A26}$$

This expression shows that the equilibrium ratio depends only upon the exchange time, the relaxation time in the target cell, and the fraction of atoms in each cell. Since these are quantities that generally are fixed for a given geometry, pressure, temperature, and beam current, this expression shows explicitly that the pumping cell polarization can be used as a monitor of the polarization in the target cell. Figure 15 shows the equilibrium ratio of polarizations in the two cells as a function to τ_t for different values of the exchange time. The target cell polarization approaches that in the pumping cell as the target cell relaxation time gets longer and as the exchange time gets shorter.

It is necessary to understand the evolution of the polarization in the two cells to determine how long the system takes to reach equilibrium so that one is sure that the polarizations have equilibrated before using the equilibrium ratio to infer the target cell polarization from the measured polarization in the pumping cell. Figure 16 is a plot of $P_t(t)/P_p(t)$, showing how quickly the system approaches equilibrium for values of the time constants similar to those for the ^{3}He target used in this experiment. In this target system equilibrium was reached after about 800 sec.

The ratio of the pumping cell equilibrium polarization to that obtainable with a single cell, P_p/P_s, is

$$\frac{P_p}{P_s} = \frac{\left(\frac{1}{T}+\frac{1}{\tau_p}\right)\left(\frac{1}{\tau_t}+\left(\frac{N_p}{N}\right)\frac{1}{t_{ex}}\right)}{\left(\frac{1}{T}+\frac{1}{\tau_p}\right)\left(\frac{1}{\tau_t}+\left(\frac{N_p}{N}\right)\frac{1}{t_{ex}}\right)+\left(\frac{N_t}{N}\right)\frac{1}{t_{ex}}\frac{1}{\tau_t}}. \tag{A27}$$

If we define the effective pumping time (a more easily measured quantity) by $\frac{1}{T_{eff}} \equiv \frac{1}{T}+\frac{1}{\tau_p}$, then the equation for the achievable pumping cell polarization in the double-cell system can be rewritten as

$$\frac{P_p}{P_s} = \frac{1}{1+\left(\frac{N_t}{N_p}\frac{T_{eff}}{\tau_t}/\left(1+\frac{N}{N_p}\frac{t_{ex}}{\tau_t}\right)\right)}. \tag{A28}$$

Figure 17 shows the ratio of the equilibrium pumping cell polarization to the polarization in a single cell of the same size, as a function of the target cell relaxation time for different values of the exchange time. Figure 18 shows the dependence upon the pumping time constant. This information can be used to predict the achievable polarization for a two-cell polarized ^{3}He target given the expected optical pumping time and relaxation rates. For example, for relaxation times typical of the polarized ^{3}He target, τ_t = 500–1500 sec, the polarization in the pumping cell of a double-cell target system was $\sim$ 75%–90% of that attained with a single cell under identical experimental conditions. Since the target cell polarization was somewhat less than the pumping cell polarization (P_t/P_p $\sim$0.95–0.90), the target polarization for the polarized ^{3}He target used in the experiment was 65%–85% of that achievable with a single cell.

[1] B. Blankleider and R. M. Woloshyn, Phys. Rev. C **29**, 538 (1984).
[2] L. Koester, W. Nistler, and W. Waschkowski, Phys. Rev. Lett. **36**, 1021 (1976).
[3] C. E. Jones-Woodward *et al.*, Phys. Rev. C **44**, R571 (1991); C. E. Woodward *et al.*, Phys. Rev. Lett. **65**, 698 (1990).
[4] T. W. Donnelly and A. S. Raskin, Ann. Phys. (N.Y.) **169**, 247 (1986).
[5] J. L. Friar, B. F. Gibson, G. L. Payne, A. M. Bernstein, and T. E. Chupp, Phys. Rev. C **42**, 2310 (1990).
[6] I. R. Afnan and N. D. Birrell, Phys. Rev. C **16**, 823 (1977).
[7] C. Ciofi degli Atti, E. Pace, and G. Salmè, in *Proceedings of the Workshop on Electronuclear Physics with Internal Targets and the BLAST Detector,* edited by R. Alarcon and M. Butler (World Scientific, Singapore, 1992).
[8] C. Ciofi degli Atti (private communication).
[9] K. Dow *et al.*, Phys. Rev. Lett. **61**, 1706 (1988); K. Dow, Ph.D. thesis, MIT, 1987.
[10] E. van Meijgaard and J. A. Tjon, Phys. Lett. B **228**, 307 (1989).
[11] G. D. Cates *et al.*, Nucl. Instrum. Methods A **278**, 293 (1989).
[12] J. Arrington *et al.*, Nucl. Instrum. Methods A **311**, 39 (1992).
[13] D. C. Carey, K. L. Brown, and C. Iselin, Decay TURTLE, A Computer Program for Simulating Charged Particle Beam Transport Systems, Including Decay Calculations, Report No. SLAC-246, 1982 (unpublished).
[14] G. B. West, Phys. Rep. C **18**, 264 (1975).
[15] F. D. Colegrove, L. D. Schearer, and G. K. Walters, Phys. Rev. **132**, 2561 (1963).
[16] L. Schearer and M. Leduc, IEEE J. Quantum. Electron. **QE22**, 756 (1986); P. Tin and L. D. Schearer, J. Appl. Phys. **68**, 950 (1990); T. R. Gentile and R. D. McKeown, Phys. Rev. A **47**, 456 (1993).
[17] K. Lee, J.-O. Hansen, J. F. J. van den Brand, and R. G. Milner, Nucl. Instrum. Methods A (submitted).
[18] D. S. Betts and M. Leduc, Ann. Phys. (Paris) **11**, 267 (1986).
[19] F. D. Colegrove, L. D. Schearer, and G. K. Walters, Phys. Rev. **135**, A353 (1964); P. J. Nacher and M. Leduc, J. Phys. (Paris) **44**, 2057 (1985).
[20] W. Heil and E. Otten (private communication).
[21] T. R. Gentile (private communication).
[22] M. Pavlovic and F. Laloë, J. Phys. **31**, 173 (1970).
[23] W. Lorenzon, T. R. Gentile, H. Gao, and R. D. McKeown, Phys. Rev. A (submitted).
[24] R. S. Timsit, J. M. Daniels, and A. D. May, Can. J. Phys. **49**, 560 (1971).
[25] R. G. Milner, R. D. McKeown, and C. E. Woodward, Nucl. Instrum. Methods A **257**, 286 (1987).
[26] K. D. Bonin, T. G. Walker, and W. Happer, Phys. Rev. A **37**, 3270 (1988).
[27] H. Gao (private communication).
[28] L. W. Mo and Y.-S. Tsai, Rev. Mod. Phys. **41**, 205 (1969).
[29] J. S. McCarthy, I. Sick, and R. R. Whitney, Phys. Rev. C **15**, 1396 (1977).
[30] S. Galster, H. Klein, J. Moritz, K. H. Schmidt, D. Wegener, and J. Bleckwenn, Nucl. Phys. **B32**, 221 (1971).
[31] M. Gari and W. Krümpelmann, Phys. Lett. B **173**, 10 (1986).
[32] A. K. Thompson *et al.*, Phys. Rev. Lett. **68**, 2901 (1992).
[33] T. E. Chupp, R. A. Loveman, A. K. Thompson, A. M. Bernstein, and D. R. Tieger, Phys. Rev. C **45**, 915 (1992).